Analysis of the failure at notches and cavities in quasi-brittle media using the Thick Level Set damage model and comparison with the coupled criterion

Jihed Zghal, Kevin Moreau, Nicolas Moës, Dominique Leguillon, Claude Stolz

Analysis of the failure at notches and cavities in quasi-brittle media using the Thick Level Set damage model and comparison with the coupled criterion

J. Zghal, K. Moreau, N. Moës, D. Leguillon, C. Stolz

Abstract The failure of quasi-brittle specimen weakened by sharp or blunted notches and cavities is analyzed under quasi-static loading. The load at failure is obtained with the Thick Level Set (TLS) damage modeling. In this model, the damage gradient is bounded implying that the minimal distance between a point where damage 0 (sound material) to 1 (fully damaged) is an imposed characteristic length in the model. This length plays an important role on the damage evolution and on the failure load. The paper shows that the TLS predictions are relevant. A comparison with the coupled criterion (CC) of Leguillon (2002) is given. A good agreement is obtained for cavities and V-notches provided that the characteristic length of Irwin is small compared to the notch depth (condition for the applicability of the CC criterion). A comparison with failure loads obtained experimentally is also given. In the numerical simulations, uniform stresses are imposed at infinity using a new finite element mapping technique (Cloirec 2005).

Keywords Damage · Failure · Thick Level Set · TLS · Coupled criterion · V-notch · Cavity

J. Zghal (✉)· K. Moreau · N. Moës · C. Stolz
GeM Institute, UMR CNRS 6183, Ecole Centrale de Nantes, 1 rue de la Noë Nantes, 44321 Nantes, France
e-mail: jihed.zghal@ec-nantes.fr

N. Moës
e-mail: nicolas.moes@ec-nantes.fr

C. Stolz
e-mail: claude.stolz@ec-nantes.fr

D. Leguillon
Institut Jean Le Rond d'Alembert, Sorbonne Universit, Centre National de la Recherche Scientifique, UMR 7190, 75005 Paris, France
e-mail: dominique.leguillon@upmc.fr

C. Stolz
IMSIA, EdF-CEA-CNRS-ENSTA Paristech UMR9219, Université Paris Saclay, 828 Boulevard des Maréchaux, 91762 Palaiseau, France

1 Introduction

Predicting the maximum load that a quasi-brittle specimen can sustain is an important scientific and practical issue. A natural approach is to search for a criterion. Strength and toughness criteria are well suited for simple specimen having either no defect or an existing long crack. When notches, or cavities are present, the criterion is more complex to set up. An example of such criteria is the coupled criterion introduced in Leguillon (2002). It is a semi-analytical approach since it starts from analytical developments finalized by a (simple) numerical treatment.

Another approach to determine maximum loads is to perform a full numerical quasi-static analysis of the specimen with an increasing loading. The failure load is defined as the maximum load above which no quasi-static solution may numerically be found (and the specimen goes into dynamic failure). The model

computed may be a cohesive zone model as in Gómez and Elices (2003) and Gómez and Elices (2004) for sharp and rounded notches. Also, one may consider damage mechanics. This is the path followed in this paper.

We consider in this paper the Thick Level Set damage model (TLS) (Moës et al. 2011). In this model the damage gradient is bounded and a characteristic length is introduced. (It is well known that a characteristic length is needed when addressing failure with a damage model, otherwise failure could be reached for an infinitely small loading.) The TLS characteristic length to minimal distance needed between a point where damage is 0 and a point where damage is 1. This TLS model bridges damage initiation, crack initiation and crack propagation in a single theory. It has been compared to the cohesive zone model in Gómez et al. (2015).

The goal of this paper is to compare the predicted failure load by the the damage approach (TLS) and the coupled criterion (CC). The role played by the different characteristic lengths in each model will also be analyzed. The coupled criterion indeed implicitly introduces a length since it is written in terms of both toughness and strength of the material. To be precise, specimen considered in this paper are semi-infinite for notches and infinite for cavities. Thus, the specimen does introduce only one length for sharp notches and cavities; and two for blunted notches (fillet radius on top of the notch depth).

The paper is organized as follows. The TLS model is presented in Sect. 2. A new point of view is adopted for the presentation. The level set ingredient is not introduced immediately but at a later stage. Providing this point of view will most likely help readers familiar with variational approach to fracture to better grasp the TLS model. The TLS implementation for the failure analysis of V-notches and cavities is then detailed in Sect. 3. In particular, the way boundary conditions are imposed at infinity is detailed. The coupled criterion approach is recalled in Sect. 4. This approach has been detailed in several papers. It is presented here in a comprehensive manner including new tables not given previously. The comparison between the TLS and CC predictions is given in Sect. 5. Finally, Sect. 6 provides a discussion and a conclusion.

2 The Thick Level-Set damage model

We first describe a simple local damage model. This model will then be modified into a non-local model through the TLS approach.

2.1 The local damage model

We consider the expression below for the free energy φ. The scalar damage is denoted d, the strain ε and the initial Hooke tensor $\mathbf{E}$:

$$\varphi(\varepsilon, d) = \frac{1}{2}(1-d)\varepsilon : \mathbf{E} : \varepsilon \tag{1}$$

State equations are obtained by differentiation:

$$\sigma = \frac{\partial \varphi}{\partial \varepsilon} = (1-d)\mathbf{E} : \varepsilon, \quad Y = -\frac{\partial \varphi}{\partial d} = \frac{1}{2}\varepsilon : \mathbf{E} : \varepsilon \tag{2}$$

The time-independent damage evolution model is described by a damage criterion f on the driving force Y:

$$f(Y, d) = Y - Y_c\, h(d) \leq 0 \tag{3}$$

The hardening function $h(d)$ is chosen such that $h(0) = 1$ and $h'(d) \geq 0$ to avoid snap-back at material level under uni-axial tension. The quantity Y_c is the critical local energy value for damage initiation. Finally, damage evolution is expressed by:

$$\dot{d} \geq 0, \quad f \leq 0, \quad f\dot{d} = 0 \tag{4}$$

The stress response of the above model to a monotonic increasing strain is a typical 1D curve depicted in Fig. 1, on which the straight elastic unloading path is also shown.

For later use, we compute the work dissipation capability for a material point. Using the following definition for the work dissipated over a time interval $[0, t]$:

$$W = \int_0^t \frac{1}{2}(\sigma : \dot{\varepsilon} - \dot{\sigma} : \varepsilon)\, \mathrm{d}t, \tag{5}$$

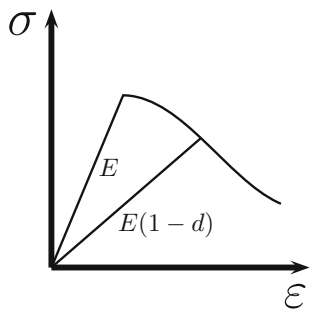

Fig. 1 Stress response for an increasing strain with a typical elasto-damage law and unloading path

we get

$$W = \int_0^t Y\dot{d}\ \mathrm{d}t = \int_0^t Y_c h(d)\dot{d}\ \mathrm{d}t$$
$$= Y_c \int_0^d h(s)\ \mathrm{d}s = Y_c \tilde{h}(d) \tag{6}$$

where $\tilde{h}$ is defined as the integral of h. Note that in the 1D setting, the work dissipated D corresponds to the curvilinear triangular area under the curve (Fig. 1) which is comprised between the initial elastic slope and the damaging response. The total work a material point can dissipate is obtained by evaluating $\tilde{h}$ at $d = 1$. We require $\tilde{h}(1)$ to be bounded. To summarize, function $\tilde{h}$ must satisfy:

$$\tilde{h} \in C^0([0,1]) \quad \text{bounded and convex:}$$
$$\tilde{h}(0) = 0,\ \tilde{h}'(0) = 1 \tag{7}$$

2.2 The Thick Level Set damage model

The model described in the preceding section is local: damage evolution at a point is driven only by the strain history at that point. Local damage models are known to be ill-posed (Bazant et al. 1984). The load needed for failure of a specimen with an initial singularity is infinitely small and so is dissipation. Local models need to be regularized to enforce some dissipation at failure. For this purpose, we change the constitutive model. A constraint is imposed on damage evolution. It was first presented in Moës et al. (2011) and later refined in Bernard et al. (2012) and Moës et al. (2014). The main idea is to constrain the norm of the damage gradient through a Hamilton–Jacobi type operator H:

$$H(d, \nabla d) = \|\nabla d\| - \frac{g(d)}{l_c} \leq 0 \tag{8}$$

where l_c is a characteristic length and $g(d)$ is a dimensionless positive concave bounded function (concavity ensures a convex admissible damage field set, Frémond and Stolz 2017). By enforcing a normalization condition on $g(d)$:

$$\int_0^1 \frac{1}{g(d)}\ \mathrm{d}d = 1 \tag{9}$$

we obtain a clear meaning for l_c. It is the smallest possible distance between a point where damage is 0 and a point where damage is 1 (the proof will be given in Sect. 2.5). Equation (8) separates the domain into two zones based on whether the constraint is active or not.

$$\Omega^- = \{\mathbf{x} \in \Omega : H < 0\}, \quad \Omega^+ = \{\mathbf{x} \in \Omega : H = 0\} \tag{10}$$

Over Ω^-, the TLS approach uses the local damage evolution equations (4). Over Ω^+, the constraint $H = 0$ is active and the inequality below must be fulfilled:

$$\dot{H} \leq 0 \tag{11}$$

The local damage evolution is no longer appropriate since it may violate the above. In the TLS approach, condition (11) is considered always as an equality, which restricts spatially the damage rate. Enforcing $\dot{H} = 0$, when $H = 0$, we get:

$$\dot{H} = \frac{\nabla d \cdot \nabla \dot{d}}{\|\nabla d\|} - \frac{g'(d)}{l_c}\dot{d}$$
$$= l_c \nabla d \cdot \left(\frac{\nabla \dot{d}}{g(d)} - g'(d)\dot{d}\frac{\nabla d}{g(d)^2}\right)$$
$$= l_c \nabla d \cdot \nabla\left(\frac{\dot{d}}{g(d)}\right) = 0 \tag{12}$$

The above condition defines an admissible set $\mathcal{A}^+$ for damage evolution:

$$\frac{\dot{d}}{g(d)} \in \mathcal{A}^+ = \{a \in L^\infty(\Omega^+) : \nabla d \cdot \nabla a = 0 \text{ over } \Omega^+\} \tag{13}$$

Equation (12) indicates that $\dot{d}/g(d)$ is uniform along the gradient of d. The space $\mathcal{A}^+$ is then used to define the projection operators from f to $\overline{f}$ and from $\dot{d}$ to $\overline{\dot{d}}$:

$$\overline{f} \in \mathcal{A}^+, \quad \int_{\Omega^+} \overline{f} g(d) a \, \mathrm{d}\Omega = \int_{\Omega^+} f g(d) a \, \mathrm{d}\Omega, \quad \forall a \in \mathcal{A}^+ \tag{14}$$

$$\overline{\dot{d}} \in \mathcal{A}^+, \quad \int_{\Omega^+} \overline{\dot{d}} a \, \mathrm{d}\Omega = \int_{\Omega^+} \dot{d} a \, \mathrm{d}\Omega, \quad \forall a \in \mathcal{A}^+ \tag{15}$$

Finally the TLS damage evolution over Ω^+ is given by (Bernard et al. 2012):

$$\overline{\dot{d}} \geq 0, \quad \overline{f} \leq 0, \quad \overline{f}\overline{\dot{d}} = 0 \tag{16}$$

The TLS damage evolution model is quite different from the local evolution model (4). Still, one can show that $\dot{d} \geq 0$ is preserved locally and $f\dot{d} = 0$ is preserved on average. Indeed we have [see Moës et al. (2014)] using (16):

$$\int_{\Omega^+} f\dot{d} \, \mathrm{d}\Omega = \int_{\Omega^+} \overline{f}\overline{\dot{d}} \, \mathrm{d}\Omega = 0 \tag{17}$$

During damage evolution, domains Ω^+ and Ω^- evolve. Let Γ denote the boundary between the two domains. The continuity of a mechanical quantity f across this boundary implies jump relations between time and space gradients of f. The jump of a quantity f at some point $\mathbf{x}$ on the interface Γ is denoted $[f]$:

$$[f](\mathbf{x}) = f^+(\mathbf{x}) - f^-(\mathbf{x}), \quad f^\pm(\mathbf{x}) = \lim_{h \to 0^+} f(\mathbf{x} \pm h\mathbf{n}(\mathbf{x})) \tag{18}$$

where $\mathbf{n}$ is the outward normal on Γ pointing toward Ω^+. Continuity of damage on Γ implies the following Hadamard condition where $\mathbf{v}$ is the velocity of Γ:

$$[\dot{d}] + \mathbf{v} \cdot [\nabla d] = 0 \tag{19}$$

It should be now clear after this section that the TLS approach is not yet another gradient damage approach. It could however be called graded damage, as pointed it out in Stolz (2016) and Frémond and Stolz (2017) since damage is enforced to fit an imposed gradient in space

2.3 Material toughness in the TLS damage model

We consider in this paper material models exhibiting only softening (no damage hardening). The damage in the diffuse zone, Ω^-, will be zero. The softening-only behavior is enforced by condition (20) (negative stress strain slope as soon as damage starts as shown in Fig. 1):

$$h(d) \geq \frac{1}{2}(1-d)h'(d) \tag{20}$$

A closed form expression for the material toughness is computed by considering an auto-similar TLS crack propagating at some speed $\dot{l}$ as shown in Fig. 2. The power dissipated is

$$D = \int_\Omega Y \dot{d} \, \mathrm{d}\Omega = \int_\Omega Y_c h(d) \dot{d} \, \mathrm{d}\Omega \tag{21}$$

The second equality comes from Eqs. (17) and (16)–(3). Using the steady state condition on damage

$$\dot{d} + \dot{l} \nabla d \cdot \mathbf{e}_x = 0 \tag{22}$$

we get:

$$D = Y_c \dot{l} \int_\Omega h(d)(-\nabla d \cdot \mathbf{e}_x) \, \mathrm{d}\Omega \tag{23}$$

The integral is decomposed into an integral along the x axis and then along the y axis (see Fig. 2). On a parallel line $\mathbf{e}_x$ at high y, damage grows from 0 to the value $d(y)$ at $x = 0$

$$\begin{aligned} D &= Y_c \, \dot{l} \int_{-l_c}^{l_c} \int_{-\infty}^{+\infty} h(d)(-\nabla d \cdot \mathbf{e}_x) \, \mathrm{d}x \, \mathrm{d}y \\ &= Y_c \, \dot{l} \int_{-l_c}^{l_c} \int_0^{d(y)} h(s) \, \mathrm{d}s \, \mathrm{d}y \\ &= Y_c \dot{l} \int_{-l_c}^{l_c} \tilde{h}(d(y)) \, \mathrm{d}y \end{aligned} \tag{24}$$

Finally, we use the condition of steady-state and the constraint $H(d) = 0$

$$\nabla d \cdot \mathbf{e}_y = -\frac{g(d)}{l_c} \tag{25}$$

to obtain the final expression:

$$D = 2Y_c \, l_c \, \dot{l} \int_0^1 \frac{\tilde{h}(d)}{g(d)} \, \mathrm{d}d. \tag{26}$$

This is a weighted average of the local material dissipation capability $\left(Y_c \tilde{h}(d)\right)$ multiplied by the damage zone thickness $2l_c$ and the crack speed.

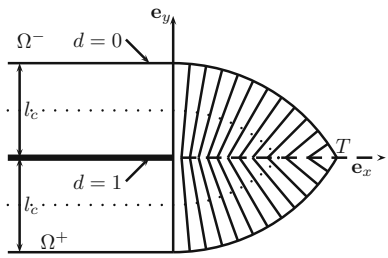

Fig. 2 Auto-similar propagation of a TLS type crack in an infinite media. Segments indicates damage gradient direction. The dotted curve is an iso-d

2.4 Link with the cohesive model

At this stage, we have not yet decided on a particular choice of the $g(d)$ function. We analyze the consequence of this choice on the critical opening at failure. Given parameters of a TLS model, a corresponding cohesive model with the same overall response in uniaxial tension may be obtained in term of traction σ and crack opening w (Gómez et al. 2015). It reads:

$$\sigma = \sigma_c \sqrt{1-d}\ \sqrt{\frac{\tilde{h}(d)}{d}} \tag{27}$$

$$w = \frac{2l_c}{E}\,\sigma \int_0^d \frac{x}{1-x}\frac{1}{g(x)}\,\mathrm{d}x \tag{28}$$

where $\sigma_c = \sqrt{2EY_c}$. The critical opening of the cohesive model as $d \to 1$ is given by:

$$\begin{aligned} w_c &= \lim_{d\to 1} w \\ &= \frac{2\sigma_c l_c}{E} \lim_{d\to 1} \left(\sqrt{\frac{\tilde{h}(d)}{d}} \sqrt{1-d} \int_0^d \frac{x}{1-x}\frac{1}{g(x)}\,\mathrm{d}x \right) \\ &= \frac{2\sigma_c l_c}{E} \sqrt{\tilde{h}(1)} \lim_{d\to 1} \left(\sqrt{1-d} \int_0^d \frac{x}{1-x}\frac{1}{g(x)}\,\mathrm{d}x \right) \\ &= \frac{2\sigma_c l_c}{E} \sqrt{\tilde{h}(1)} \lim_{d\to 1} \frac{2\sqrt{1-d}}{g(d)} \end{aligned} \tag{29}$$

The last equality has been obtained by the L'Hospital theorem. The critical opening is thus governed by the asymptotic behaviour of $g(d)$ as $d \to 1$. To avoid zero or infinite critical opening, g must behave asymptotically as a square root function. We decide to pursue with the simplest choice satisfying the normalization condition (9):

$$g(d) = 2\sqrt{1-d} \tag{30}$$

2.5 Geometrical interpretation and implementation of the TLS model

At this stage we describe the geometrical content and its relationship with level set technology which drives the implementation (Sethian 1999). We introduce the level set function ϕ defined by:

$$\phi(d) = l_c \int_0^d \frac{1}{g(s)}\,\mathrm{d}s \tag{31}$$

As damage grows from 0 to 1, the level set rises monotoneously from 0 to l_c. Replacing d by ϕ as unknown in (8), we obtain a simpler expression

$$\|\nabla\phi\| - 1 \le 0 \tag{32}$$

Over Ω^+, the condition is:

$$\|\nabla\phi\| = 1 \tag{33}$$

which is known as the eikonal equation. The above equation must be understood in the sense of limit viscosity solution as defined by Lions (1982). Solution ϕ is obtained by passing to the limit as $\epsilon \to 0$ with respect to solutions ϕ^ϵ of the following non-linear elliptic equation:

$$\|\nabla\phi^\epsilon\| - 1 - \epsilon\Delta\phi^\epsilon = 0 \quad \epsilon > 0 \tag{34}$$

where Δ is the Laplace operator. The limit has an explicit expression in terms of the boundary values (Lions 1982):

$$\phi(\mathbf{x}) = \min_{\mathbf{y}\in\partial\Omega^+} (\phi(\mathbf{y}) + L(\mathbf{x},\mathbf{y})), \quad \mathbf{x} \in \Omega^+ \tag{35}$$

where $L(\mathbf{x},\mathbf{y})$ is the length of the shortest path, contained in Ω^+, linking points $\mathbf{x}$ and $\mathbf{y}$. If the boundary data are zero, ϕ is simply the distance function to the boundary. Equations (31) and (35) completely characterize the d field over Ω^+. Equation (35) implies that ϕ is continuous. Its gradient is however not continuous. The set of points for which the gradient is discontinuous is called the skeleton of Ω^+ and denoted Γ_s. The skeleton of the damage zone emanating from a notch is the segment OT in Fig. 3. The skeleton is the set of points $\mathbf{x} \in \Omega^+$ where arguments $\mathbf{y}$ in (35) are not unique.

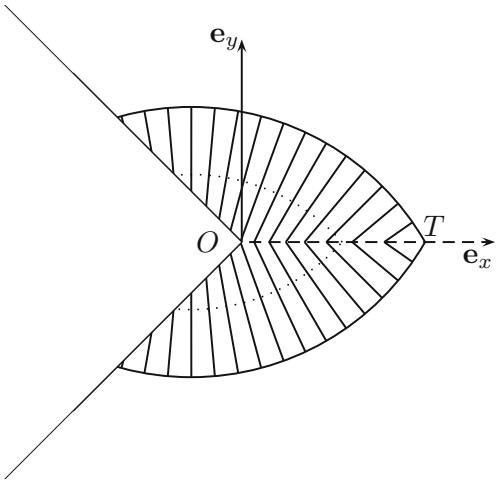

Fig. 3 Sketch of the damage extent around a V-notch with the TLS approach. Point T indicates the tip of the damage zone along the notch bisector. Segments indicate the damage gradient direction within the damage zone

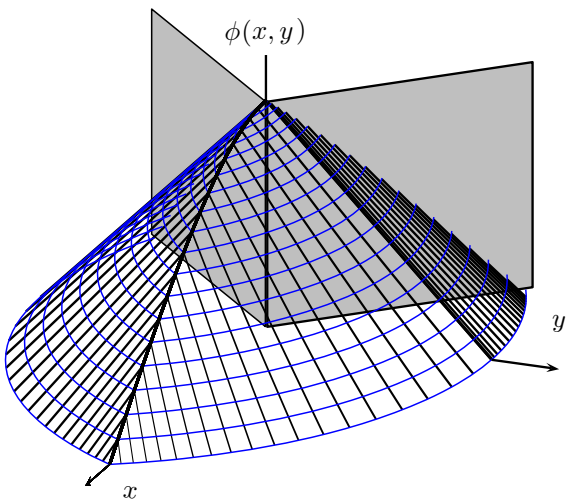

Fig. 4 Same as previous figure but showing damage with elevation

Over Ω^+, the ϕ field has a simple geometrical interpretation. Its elevation is a ruled surface (except on the skeleton). Gradients of ϕ are organized along segments joining the boundary of Ω^+ to the skeleton (see Figs. 3 and 4).

Condition (12) and relation (35) imply that the level set field velocity is uniform along the gradient of d (depicted on Fig. 2):

$$\nabla d \cdot \nabla \phi = 0 \tag{36}$$

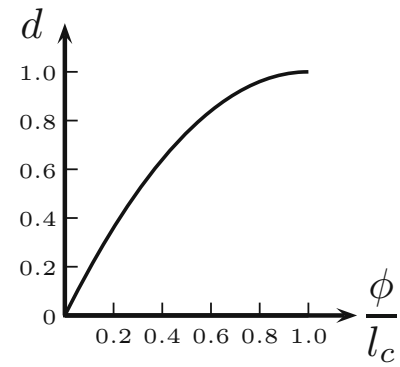

Fig. 5 Damage profile considered in this paper

We are now able to prove the fact that under condition (8) (or equivalently (32)) the distance between a point where $d = 0$ and a point where $d = 1$ is at least l_c. It is the same as proving that the distance between a point where $\phi = 0$ and a point where $\phi = l_c$ is at least l_c. This is obvious from (35).

Since function $\phi(d)$ is monotoneously increasing, it can be inverted to give the so-called damage profile $d(\phi)$. The choice (30) for $g(d)$ corresponds to the following profile:

$$R^+ \to R^+ : d(\phi) = \begin{cases} 0 & \text{if } \phi \\ 1 - (1 - \phi/l_c)^2 & \text{if } 0 \le \phi \le l_c \\ 1 & \text{if } \phi \ge l_c \end{cases} \tag{37}$$

shown in Fig. 5.

3 Simulation with the TLS model

The TLS model detailed in the previous section is applied for the simulation on three types of unbounded specimen under plane strain assumptions: edge sharp or blunted notches (Fig. 6) and cavities (Fig. 7). The notch depth is denoted a and the root radius ρ. The cavity radius is also denoted ρ. The loading is a uniform tension at infinity. Material parameters corresponds to PMMA whereas the TLS parameters are those of a linear cohesive law (see "Appendix A").

The numerical implementation of the TLS model is not described here. Details may be found in Moreau et al. (2017). In the TLS simulation, the load is not imposed but obtained from a dissipation control algo-

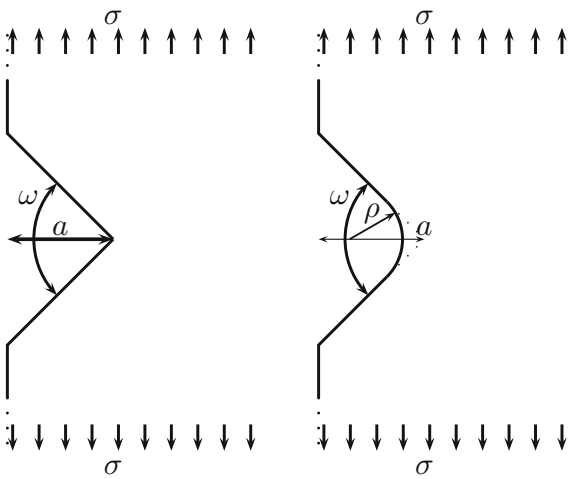

Fig. 6 Sharp (left) and blunted (right) V-notch specimen loaded at infinity

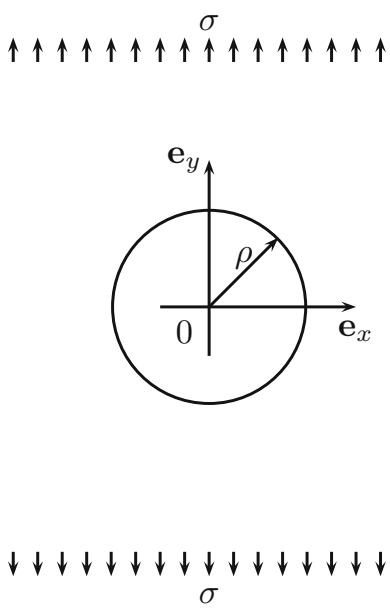

Fig. 7 A cavity in a uniaxial loaded unbounded domain

rithm. The stress at failure is recorded as the maximum load reached during the simulation. The fact that the specimen is unbounded is taken into account as follows. The domain depicted in Fig. 8 (with a sharp or blunted notch) is meshed. The radius R_2 is then sent to infinity by a geometrical mapping while radius R_1 is held fixed. The solution is sought as the sum $\mathbf{u} + \mathbf{u}_V$. Zero Dirichlet boundary conditions are imposed on $\mathbf{u}$ on the layer $r = R_2$. The given displacement $\mathbf{u}_V$ is

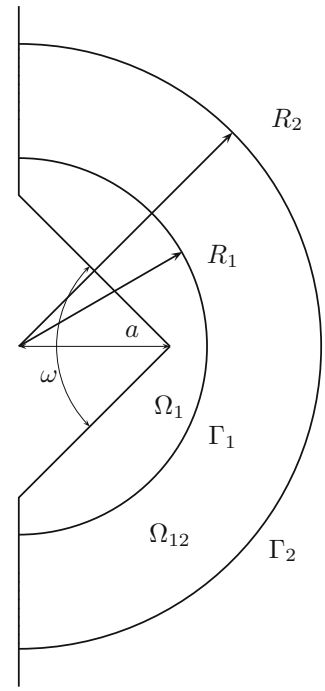

Fig. 8 Infinite domain mapping description

assumed to be such that the stress $\mathbf{E} : \varepsilon(\mathbf{u}_V)$ is divergence free. In the outer zone, the mapping is given by:

$$\mathbf{x} = \frac{R_1}{R}\left(\frac{R_2 - R_1}{R_2 - R}\right)^{1/m}\mathbf{X}, \quad R = \sqrt{X^2 + Y^2} \tag{38}$$

To understand how the mapping works, consider the 1D case. The last element is located on the segment $[R_h, R_2]$. Over this element, the displacement reads:

$$u = U_1 \frac{X_2 - X}{X_2 - X_h} \tag{39}$$

since $U_2 = 0$ (zero boundary condition on the outer layer). The mapping gives:

$$x = X_1 \left(\frac{X_2 - X_1}{X_2 - X}\right)^{1/m} \tag{40}$$

So, the displacement as a function of x reads:

$$u = U_1 \frac{X_2 - X_1}{X_2 - X_h}\left(\frac{X_1}{x}\right)^{m} \tag{41}$$

showing that the displacement decreases as a power of m. Since we are dealing with 2D problems, the best choice for m is 1.

The reason for considering a notch in a semi-infinite media and not an infinite media, is that uniform stress at infinity applied to a notch in an infinite media gives an infinite generalized stress intensity factor. Still, we could have considered the loading as the first term of the William's series for a notch in an infinite media. The problem of this scenario is that the loading which is now the GSIF (Generalized stress intensity factor) itself does not in general reach a finite maximum since, as damage increases, the loading always centered on the initial notch tip is becoming less and less harmful. Regarding the cavity case, a full disk of radius R_2 is meshed and R_2 is sent to infinity by the geometrical mapping.

For a given damage distribution, the displacement solution $\mathbf{u}$ is characterized by the variational equality: find $\mathbf{u} \in \mathcal{U} = \{\mathbf{v} \text{ on } \Omega : \mathbf{v} = 0 \text{ on } \Gamma_2\}$ satisfying

$$\int_\Omega (1-d)\varepsilon(\mathbf{u}_V + \mathbf{u}) : \mathbf{E} : \varepsilon(\mathbf{u}^*)\, \mathrm{d}\Omega = 0, \quad \forall \mathbf{u}^* \in \mathcal{U} \tag{42}$$

Since no damage takes place in the layer between R_1 and R_2 , Eq. (42) may be transformed into:

$$\begin{aligned} &\int_{\Omega_1} (1-d)\varepsilon(\mathbf{u}_V + \mathbf{u}) : \mathbf{E} : \varepsilon(\mathbf{u}^*)\, \mathrm{d}\Omega \\ &\quad + \int_{\Omega_{12}} \varepsilon(\mathbf{u}) : \mathbf{E} : \varepsilon(\mathbf{u}^*)\, \mathrm{d}\Omega \\ &= \int_{\Gamma_1} (\mathbf{E} : \varepsilon(\mathbf{u}_V)\ \mathbf{n} \cdot \mathbf{u}^*\, \mathrm{d}\Gamma, \quad \forall \mathbf{u}^* \in \mathcal{U} \end{aligned} \tag{43}$$

where $\mathbf{n}$ is the outward normal to Γ_1. The transformation reduces integration error since it avoids the integration of the imposed solution in the layer Ω_{12}. The uniform strain state $\varepsilon(\mathbf{u}_V)$ corresponds to the prescribed stress. The only non-zero components of the strain are : $-\nu\sigma/E$ and σ/E for the xx and yy components, respectively.

4 The coupled criterion

In this section we recall the main results for the coupled criterion proposed in Leguillon (2002) and Leguillon and Yosibash (2003) to predict failure at notches or cavities.

4.1 The sharp V-notch

We consider a sharp V-notch with an opening angle ω ($0 \leq \omega \leq \pi$) under plane strain in linear elasticity. The material is characterized by the Young modulus E (MPa) and Poisson ratio ν. The fracture in uni-axial tension of a homogeneous bar defines the tensile strength σ_c (MPa) and the propagation of a crack defines the toughness G_c (MPa m). Only the symmetric loading case is considered in this paper.

William's expansions (Williams 1952) of displacement and stress fields $\mathbf{U}$ and σ in the vicinity of a sharp V-notch are given by:

$$\begin{cases} \mathbf{U}(x_1, x_2) = \mathbf{c} + k_{CC}\, r^\lambda \mathbf{u}(\theta) + \cdots \\ \sigma(x_1, x_2) = k_{CC}\, r^{\lambda-1} \mathbf{s}(\theta) + \cdots \end{cases} \tag{44}$$

where $\mathbf{c}$ is an irrelevant constant (rigid motion) and k_{CC} is the generalized stress intensity factor (GSIF) with dimension $\left(\text{MPa m}^{1-\lambda}\right)$. For stress free faces of the notch, the exponent λ depends on the opening ω, as solution of an eigenvalue problem; $\mathbf{u}$ is the associated eigenmode and $\mathbf{s}$ derives from $\mathbf{U}$ through Hooke's law. The dependence of λ on the opening angle ω is given in Tables 2 and 3.

When $\omega = 0$, $\lambda = 1/2$, the notch is a crack and we denote its stress intensity factor by K_I. The critical value K_c is the value of K_I for which the crack begins to propagate in pure mode I. The critical stress intensity factor K_c is related to the toughness G_c by Irwin's relation (Irwin 1968):

$$K_c = \sqrt{\frac{E G_c}{(1-\nu^2)}} \tag{45}$$

whereas the characteristic length stemming from a dimensional analysis is:

$$l_{ch} = \frac{E G_c}{\sigma_c^2} \tag{46}$$

In the above, as we do only consider the symmetric loading case, additional terms in the expansion are not singular. The mode $\mathbf{u}$ is an even function of the polar angle θ and is normalized such that $s_{\theta\theta}(\theta = 0) = 1$. The normalization choice allows to interpret k_{CC} as the applied normal traction, σ_∞, when $\omega = \pi$, but differs by a coefficient $1/\sqrt{2\pi}$ from the usual stress intensity

factor K_I when $\omega = 0$ (See "Appendix B"). Note that a different normalization is proposed in Carpinteri et al. (2008), where k and K_I are identical when $\omega = 0$ but this normalization introduces a little more complexity in the calculations.

For the chosen normalization, the coupled criterion gives the critical GSIF k_{CC} as proposed in (Leguillon 2002):

$$k_{CC}(\omega) = \left(\frac{EG_c}{A^\star(\omega)(1-\nu^2)} \right)^{1-\lambda} \sigma_c^{2\lambda-1} \tag{47}$$

We note that the critical value depends on the opening angle ω. Details on dimensionless $A^\star$ coefficient may be found in the 1. This scaling coefficient is obtained from an asymptotic procedure carried out with respect to the small crack extension length at initiation (Leguillon 2002). To be rigorous an explicit dependence of $A^\star$ with ν should be written in (47). This fact is omitted because it is quite independent of ν in a large range of values (up to the third digit at least for $0.1 \leq \nu \leq 0.4$ as numerically checked). Note that the computed $A^\star(0)$ is close to 2π (keep in mind the selected normalization) within less than one percent.

The coupled criterion predicts a crack length at initiation of failure equal to l_{CC} given by:

$$l_{CC}(\omega) = \frac{EG_c}{A^\star(\omega)(1-\nu^2)} \frac{1}{\sigma_c^2} \tag{48}$$

This length l_{CC} is only an intermediate step in establishing the criterion (47). The above reasoning holds true provided l_{CC} is small compared to the dimensions of the structure and the notch depth. This smallness is to be checked retrospectively.

4.2 The blunted V-notch

When the V-notch root is slightly rounded, the analysis becomes more tricky (Leguillon and Yosibash 2003; Picard et al. 2006). The analysis introduces two small parameters: the notch root radius ρ and the crack length at initiation l_{CC}. We introduce the dimensionless crack length ζ:

$$\zeta = \frac{l_{CC}}{\rho} \tag{49}$$

We consider that ρ and l_{CC} are in the same order of magnitude. If not, we fall into a simpler case:

- if ρ is far greater than l_{CC} (both remaining small compared to the structure size) then ζ is small and the problem is akin to a crack initiation at a straight edge, a second expansion with respect to ζ leads to the inner-inner problem to a crack with length 1 emanating from a straight edge (infinite curvature radius).
- if l_{CC} is far greater than ρ, then the first expansion should be conducted with respect to l_{CC}, the new dimensionless parameter (the dimensionless root radius now) $1/\zeta$ is small and the problem amounts to a crack nucleation at the root of a sharp V-notch.

For a blunted V-notch, the crack initiation length is no longer given explicitly by (48) but is the solution to a nonlinear equation [keep in mind (49)]:

$$\begin{aligned} l_{CC} &= \frac{EG_c}{B^\star(\omega,\zeta)(1-\nu^2)} \frac{1}{\sigma_c^2} \\ &= \frac{EG_c}{B^\star(\omega, l_{CC}/\rho)(1-\nu^2)} \frac{1}{\sigma_c^2} \end{aligned} \tag{50}$$

Here, $B^\star$ plays the same role as $A^\star$ in Sect. 4.1, but depends now on l_{CC} through ζ. Values of $B^\star$ and $C^\star$ can be found in 1. Again, this scaling coefficient is derived from an asymptotic procedure. It is carried out with respect to the root radius ρ and ζ is a variable parameter. Indeed, in a numerical simulation, it is easier to change the dimensionless crack length ζ by relaxing the cohesion along the crack path than to vary the notch root radius, which requires change of geometry and then remeshing.

Theoretically both procedures lead to the same results, provided the two small parameters are of the same order of magnitude. It is emphasized that this equation involves the root radius ρ (not some dimensionless ratio) and that this dependence is at the origin of a size effect (Leguillon et al. 2007). Once Eq. (50) is solved, the coupled criterion leads to a critical value k'_{CC} of the dimensionless GSIF:

$$k'_{CC}(\omega) = \left(\frac{EG_c}{B^\star(\omega,\zeta)(1-\nu^2)} \right)^{1-\lambda} \sigma_c^{2\lambda-1} C^\star(\omega,\zeta) \tag{51}$$

where $\zeta = l_{CC}/\rho$ and where $C^\star$ is a known function of its variables which can be determined numerically in the same way as for $A^\star$ and $B^\star$ (1).

The root radius blunts the V-notch and increases the load at fracture. This influence tends to decrease with the opening angle ω, it is more important for small openings and disappears as $\omega \to \pi$, i.e. when there is no longer any stress concentration (Picard et al. 2006).

4.3 The cavity

We investigate the case of a cavity under uniform load at infinity. There are two main failure modes for a cavity:

(i) under tension with two cracks perpendicular to the tensile loading,
(ii) under compression with two cracks parallel to the compression direction.

In both case, the situation is very similar to the previous one with two small parameters: the radius of the cavity ρ (instead of the notch root radius) and the crack length at initiation l_{CC}.

For a cavity there is no singularity and $\lambda = 1$ (Leguillon et al. 2007), William's expansion of the elastic solution writes:

$$\begin{cases} \mathbf{U}(x_1, x_2) = \mathbf{c} + k''_{\mathrm{CC}}\, r\, \mathbf{t}(\theta) + \cdots \\ \sigma(x_1, x_2) = k''_{\mathrm{CC}}\, \tau(\theta) + \cdots \end{cases} \tag{52}$$

Note that the generalized GSIF k''_{CC} is nothing but σ_∞, the tensile or compressive stress acting at infinity.

Since the root radius and the radius of the cavity play the same role in the asymptotic expansions, notations of the preceding sections are kept. The dimensionless crack length ζ given by (49). Regarding l_{CC}, it is the solution to the nonlinear equation (53). It is a relationship very similar to (50), replacing $B^\star$ with either $B^{\star \mathrm{t}}$ for tension or $B^{\star \mathrm{p}}$ for compression (see "Appendix D").

$$\begin{aligned} l_{\mathrm{CC}} &= \frac{EG_{\mathrm{c}}}{B^{\star \mathrm{t/p}}(\zeta)(1-\nu^2)} \frac{1}{\sigma_{\mathrm{c}}^2} \\ &= \frac{EG_{\mathrm{c}}}{B^{\star \mathrm{t/p}}(l_{\mathrm{c}}/\rho)(1-\nu^2)} \frac{1}{\sigma_{\mathrm{c}}^2} \end{aligned} \tag{53}$$

Then the equivalent to (51) with $\lambda = 1$ still holds true but takes the simplified form:

$$k''_{\mathrm{CC}} = \frac{\sigma_{\mathrm{c}}}{C^{\star \alpha}(\zeta)} \tag{54}$$

where for tension $\alpha = t$:

$$C^{\star \mathrm{t}}(\zeta) = 1 + \frac{1}{2}\left[\left(\frac{1}{1+\zeta}\right)^2 + 3\left(\frac{1}{1+\zeta}\right)^4\right] \tag{55}$$

and for compression $\alpha = p$:

$$C^{\star \mathrm{p}}(\zeta) = -\frac{1}{2}\left[\left(\frac{1}{1+\zeta}\right)^2 - 3\left(\frac{1}{1+\zeta}\right)^4\right] \tag{56}$$

These values are tabulated in Tables 8 and 9 for consistency. Equation (54) is strictly equivalent to the equality given in Leguillon et al. (2007).

5 Comparison between the coupled criterion and the TLS approach

In this section, we compare the coupled criterion and the TLS approaches. They will be compared through the apparent strength.

The apparent TLS strength is defined as the highest loading that the structure can reach in a quasi-static process (Figs. 9, 10). The TLS implementation uses a dissipation control algorithm. At every step, the loading is unknown and must be found so that a given (user-data) level of work is dissipated (Moreau et al. 2017). So, the loading may increase and then decrease to keep a quasi-static process as shown in Figs. 9 and 10.

For the CC criterion, the notch critical GSIF is given by (47) or (51). It is transformed into apparent strength through the formula (57) (see "Appendix B"). For cavities, the apparent CC strength is directly given by (54).

$$\sigma_{CC} = \frac{k_{\mathrm{CC}}}{\kappa a^{1-\lambda}} \tag{57}$$

Through the comparison, we will show the influence of the defect size (depth of V-notches and radius of cavities) on the stress at failure. All apparent strength values obtained by the coupled criterion or TLS are normalized by the strength of a sound structure (without defects) defined by:

$$\sigma_c^{tr} = \frac{\sigma_c}{\sqrt{1-\nu^2}} \tag{58}$$

We will refer to the above quantity as the unnotched critical stress.

5.1 The sharp V-notch

The sharp V-notch is defined by an opening angle ω and its depth denoted a (Fig. 6) . We introduce the dimensionless ratio $\eta = a/l_{\mathrm{ch}}$. We refer to this quantity as

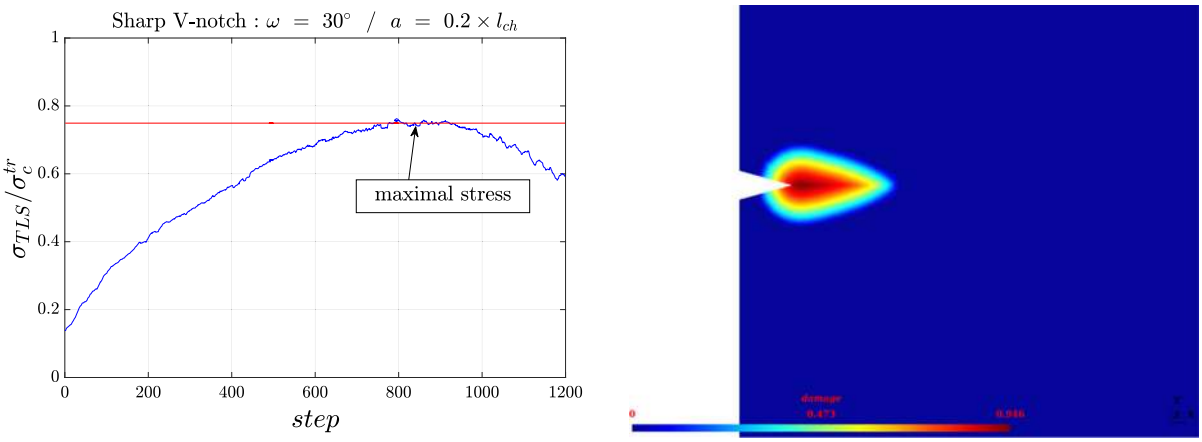

Fig. 9 Evolution of the applied stress with the step for a Sharp V-notch: **a** $\omega = 30 - \dfrac{a}{l_{ch}} = 0.2$ and **b** the damage field at the apparent strength

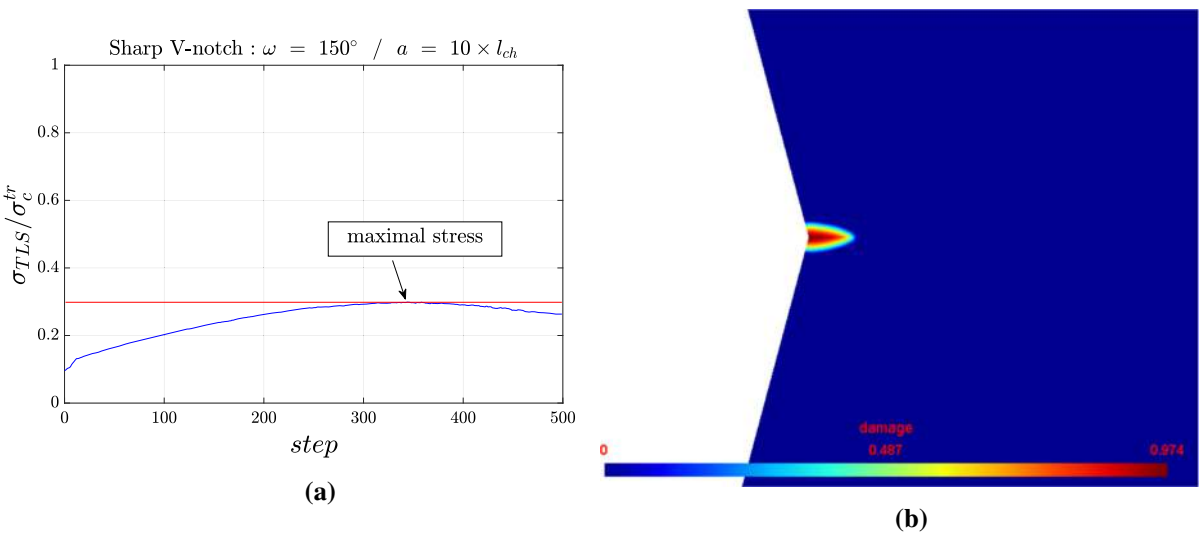

Fig. 10 Evolution of the applied stress with the step for a Sharp V-notch: **a** $\omega = 150 - \dfrac{a}{l_{ch}} = 10$ and **b** the damage field at the apparent strength

the relative notch depth. The ratio between the apparent strength obtained by the TLS and coupled criterion approach ($\sigma_{\mathrm{TLS}}/\sigma_{\mathrm{CC}}$) as a function of the relative notch depth η for angles $\omega = 30, 60, 90, 120$ and 150 degrees is presented in Fig. 11.

The comparison shows that the larger the ratio $\eta = a/l_{\mathrm{ch}}$, the closer predictions of TLS and CC are. On the other hand, when the relative notch depth η become smaller the apparent strength predicted with the CC overestimates the ones obtained by TLS (Fig. 11). Note that this is not a surprise since the CC is an asymptotic approach only valid for large notch depths compared to the material characteristic length.

According to Fig. 12, when the relative notch depth is small, the TLS apparent strength becomes closer and closer to the unnotched critical stress. This means that when the sharp V-notch depth is small compared to the characteristic length of the material, it no longer alters the structural strength. On the contrary, when the relative notch depth becomes large (i.e. the notch depth

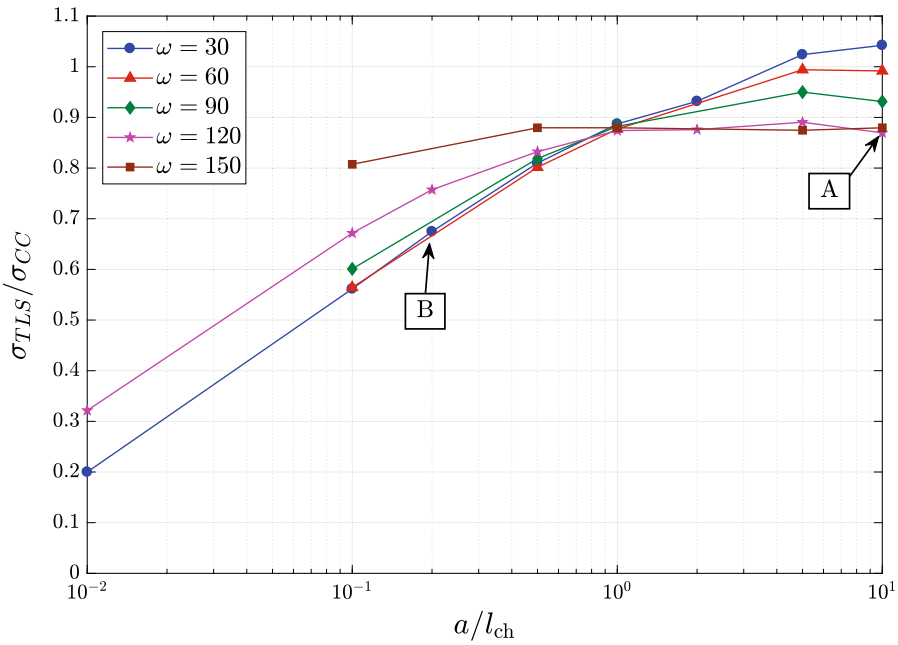

Fig. 11 Ratio of the apparent strengths ($\sigma_{\mathrm{TLS}}/\sigma_{\mathrm{CC}}$) for sharp V-Notch using the TLS approach and predicted by the coupled criterion with respect to the relative notch depth η. A and B results corresponds to Figs. 9 and 10 respectively

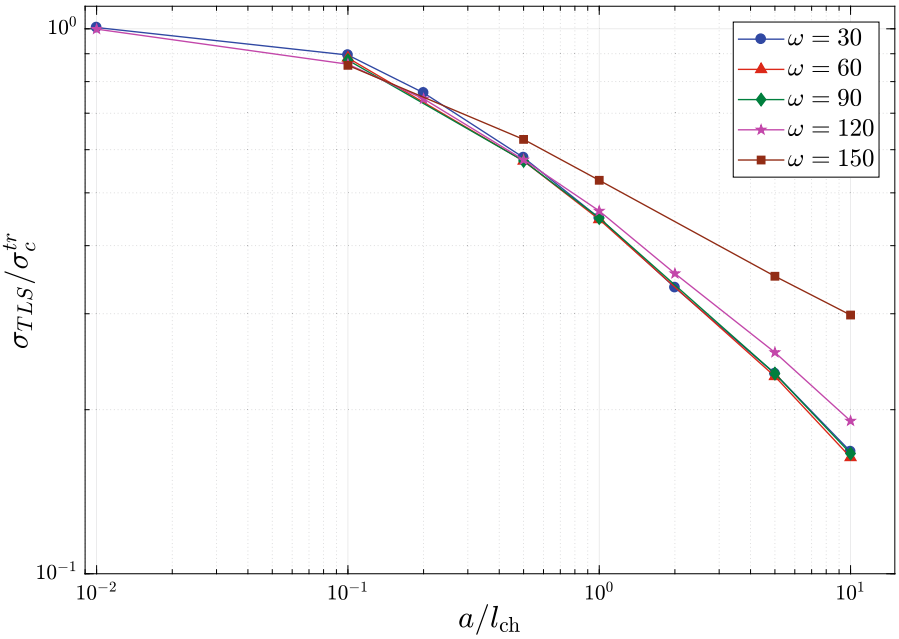

Fig. 12 Ratio between the TLS apparent strength of a sharp V-notch and the unnotched critical stress as a function of the relative notch depth

is larger than the characteristic length of the material) the apparent strength becomes smaller compared to the apparent strength of the un-notched structure.

We note also, Fig. 13, that the TLS apparent strength gets closer to the unnotched critical stress when the opening angle gets larger. In fact, when the opening angle ω is large the notch can be assimilated to a straight free edge which explains why the apparent strength is close to the unnotched critical stress. On the contrary, when ω is small, the sharp V-notch can be assimilated to a crack and the apparent strength is smaller than the unnotched critical stress.

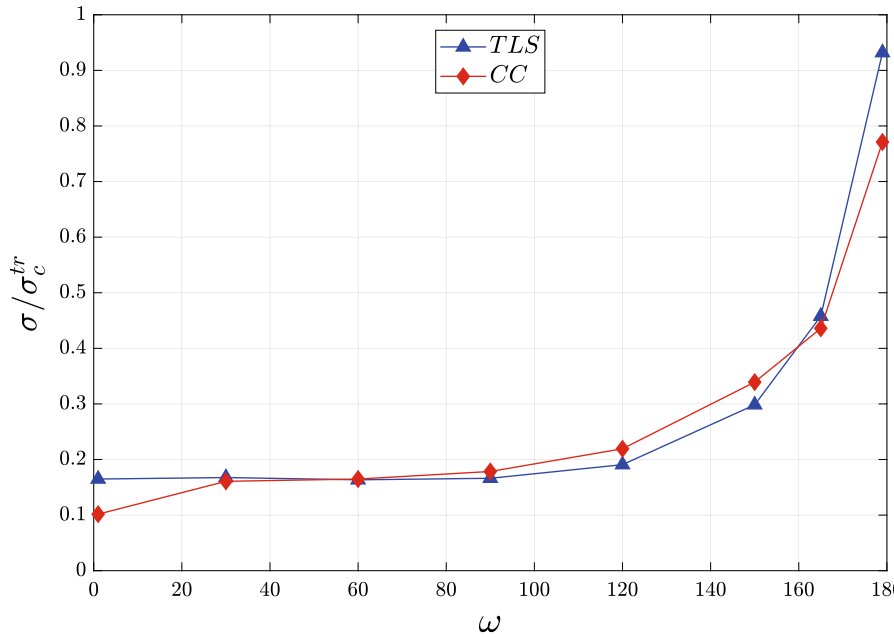

Fig. 13 Apparent strength with respect to the opening angle ω for a fixed relative notch depth ($a/l_{\text{ch}} = 10$)

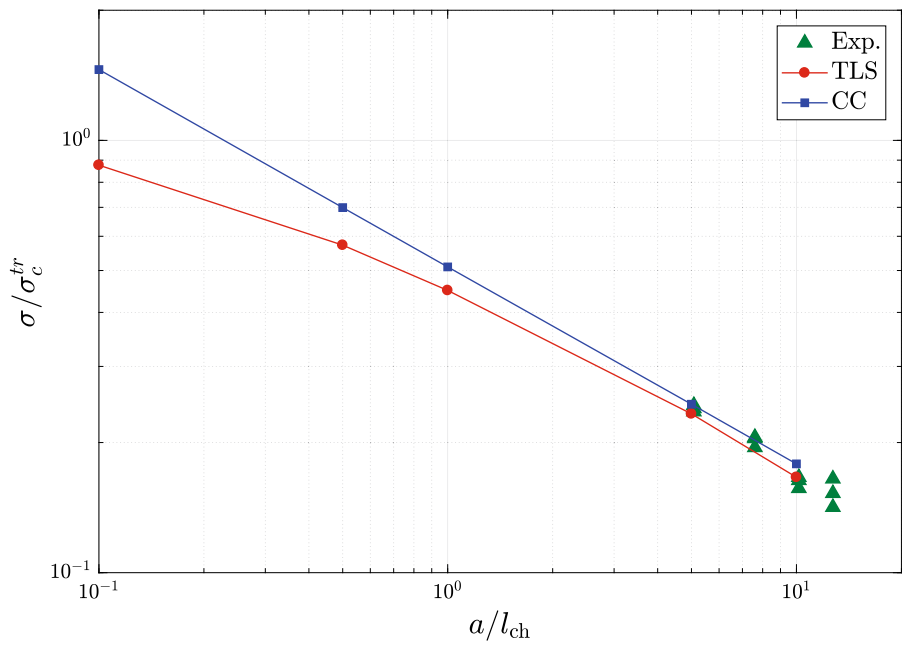

Fig. 14 V-sharp notch apparent strength obtained by CC and TLS compared with those obtained experimentally (Dunn et al. 1997) as a funtion of relative notch depth η ($\omega = 90$)

Finally, the CC and TLS predictions for a straight notch are compared to experimental data[1] in Fig. 14. The results agree pretty well.

[1] Sample sizes used for experiment are large enough to consider that notches are in semi-infinite media.

5.1.1 Influence of hardening function $\tilde{h}(d)$ on the TLS prediction

We study this influence either by keeping a given relative notch depth (η) or by keeping a given notch depth (a). The results are given in Table 1. The chosen hardening functions correspond to six different cohesive zone models depicted in Fig. 16. The six mate-

Table 1 Apparent strength for V-sharp notch prediction using different hardening functions

	(PMMA)					
	Case 1	Case 2	Case 3	Case 4	Case 5	Case 6
E [MPa]	3500					
ν	0.3					
σ_c [MPa]	70	70	35	70	35	70
$w_c \times 10^{-5}$ [m]	1	1.75	1	0.5	0.5	1.75
w_1/w_c	–	0.4	–	–	–	0.571
w_k/w_c	–	0.286	–	–	–	0.286
$G_c \times 10^{-4}$ [Mpa m]	3.5	3.5	1.75	1.75	0.875	4.25
$G_f \times 10^{-4}$ [Mpa m]	–	2.45	–	–	–	3.5
$l_{ch} \times 10^{-4}$ [m]	2.5	2.5	5	1.25	2.5	3.04
$\omega = 30°$						
$a \times 10^{-5}$ [m]	5	5	10	2.5	5	5
$\eta = \frac{a}{lch}$	0.2	0.2	0.2	0.2	0.2	0.165
σ [MPa]	55.866	52.287	27.253	59.126	27.742	55.957
σ/σ_c^{tr}	0.761	0.713	0.743	0.806	0.756	0.763
$\omega = 150°$						
$a \times 10^{-3}$ [m]	2.5	2.5	5	1.25	2.5	2.5
$\eta = \frac{a}{lch}$	10	10	10	10	10	8.235
σ [MPa]	21.913	20.068	10.741	22.870	10.956	21.964
σ/σ_c^{tr}	0.299	0.273	0.293	0.312	0.299	0.299

rial models share the same unnotched critical stress or toughness or both. Case 1 corresponds to the model used so far.

Based on results in Table 1, we note that:

- Independently of the choice of hardening function, the evolution of apparent strength as a function of the relative notch depth is not affected and all the previous conclusions remains (Fig. 15).
- For bilinear cohesive model (Case2 and 6), we notice that failure (cross in Fig. 16) corresponds to the first part of the cohesive bilinear law (Fig. 16b, f). We conclude that the primary toughness G_f is more relevant than the global toughness to predict failure. The primary toughness is then defined by (Gómez 2015):

$$G_c = G_f + \frac{1}{2}\sigma_k \left(w_c - w_1\right) \tag{59}$$

$$G_f = \frac{1}{2}\sigma_c w_1 \tag{60}$$

  For linear cohesive models the global toughness can be considered as the primary one $\left(G_c = G_f\right)$.
- If we consider the same specimen (Case 1, 2, 5 and 6), we note that the weakest is the one with the smallest apparent strength, followed by the one with the smallest primary toughness.

5.2 The blunted V-notch

We focus now on the blunted V-notch which is defined by an opening angle ω, a depth denoted a and a fillet radius ρ (Fig. 6). All studied blunted V-notches have the same depth ($a = 100 \times l_{\text{ch}}$) but different angles ω and fillet radii. We define the relative fillet radius as the ratio between the fillet radius and the material characteristic length.

A comparison between the apparent strengths obtained by the coupled criteria and the TLS approaches is given in Fig. 17. We see that when the relative fillet radius becomes small, the predicted apparent strength using the TLS approach is close to the one obtained

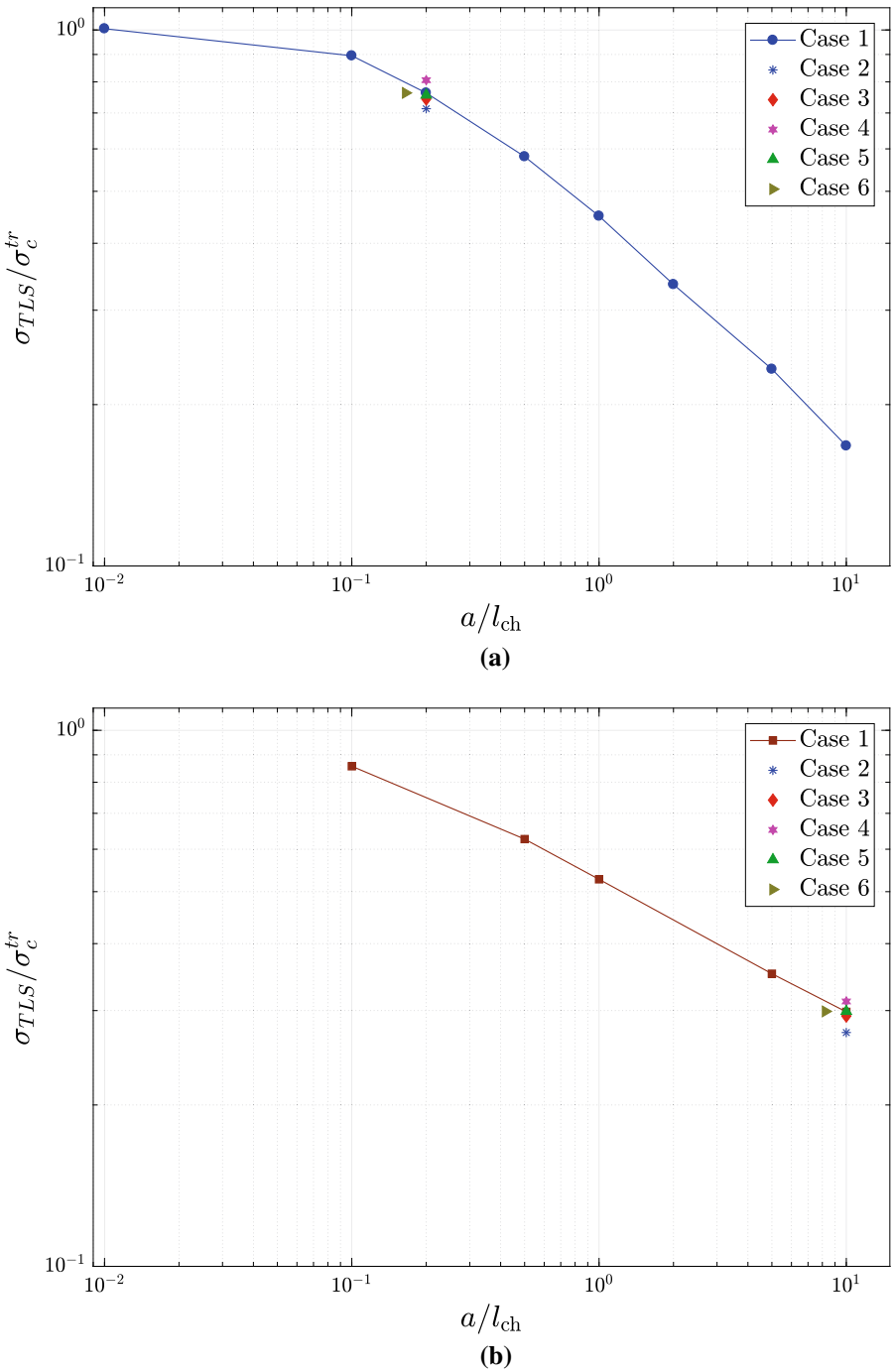

Fig. 15 Ratio between the TLS apparent strength of a sharp V-notch and the unnotched critical stress as a function of the relative notch depth: comparison between different hardening functions. **a** $\omega = 30°$, **b** $\omega = 150°$

by the coupled criterion. Indeed, when the relative fillet radius becomes small the fillet loses it's influence on the structural strength and the blunted V-notch can be assimilated to a sharp one. When the relative fillet radius becomes large, the coupled criterion underestimates the predicted TLS apparent strength.

In Fig. 18, the TLS apparent strength is also compared to the unnotched critical stress. The TLS apparent strength gets closer to the unnotched critical stress

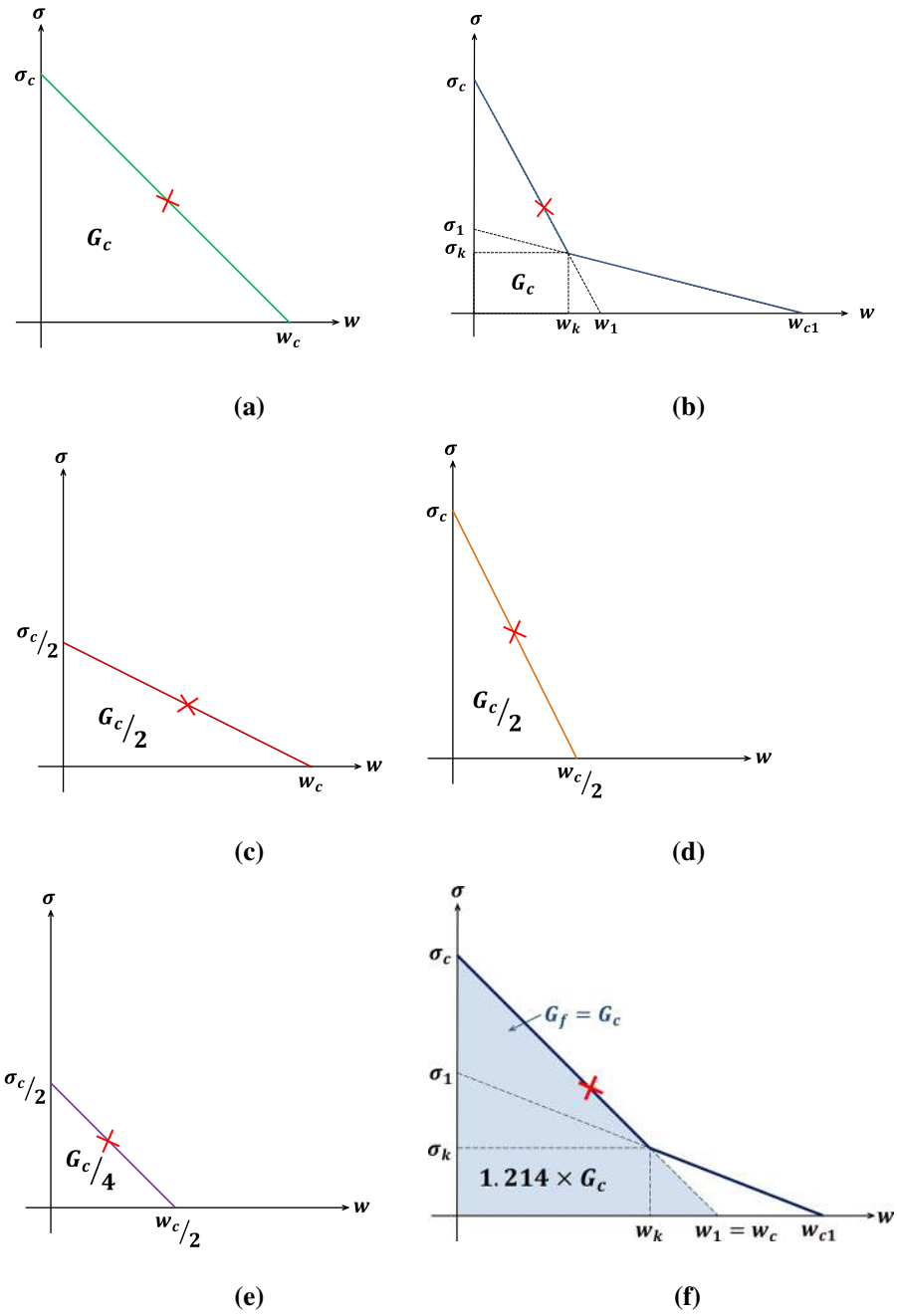

Fig. 16 The six different material models considered in Table 1. The cross corresponds to the material state at failure at the location of the highest damage. **a** Case1 (PMMA), **b** Case 2, **c** Case 3, **d** Case 4, **e** Case 5, **f** Case 6

when the fillet radius becomes large. This is even more clear for large opening angles. Indeed, in this case, the notch is even closer to a free edge scenario. The effect of the blunting is clearly shown in Fig. 19. It cleary improves the apparent strength. It is also more effective for small than large angles. This was already observed for the CC criteria (Leguillon et al. 2007).

To check if the TLS prediction is relevant when the relative fillet radius is large. We consider two cases denoted A and B in Figs. 17, 18 and 19. Case A corresponds to a fillet radius of 1/4 of the notch depth (the notch looks like a half cavity). Case B, corresponds to a fillet radius about 15 times larger than the notch depth (the notch is then basically not there anymore).

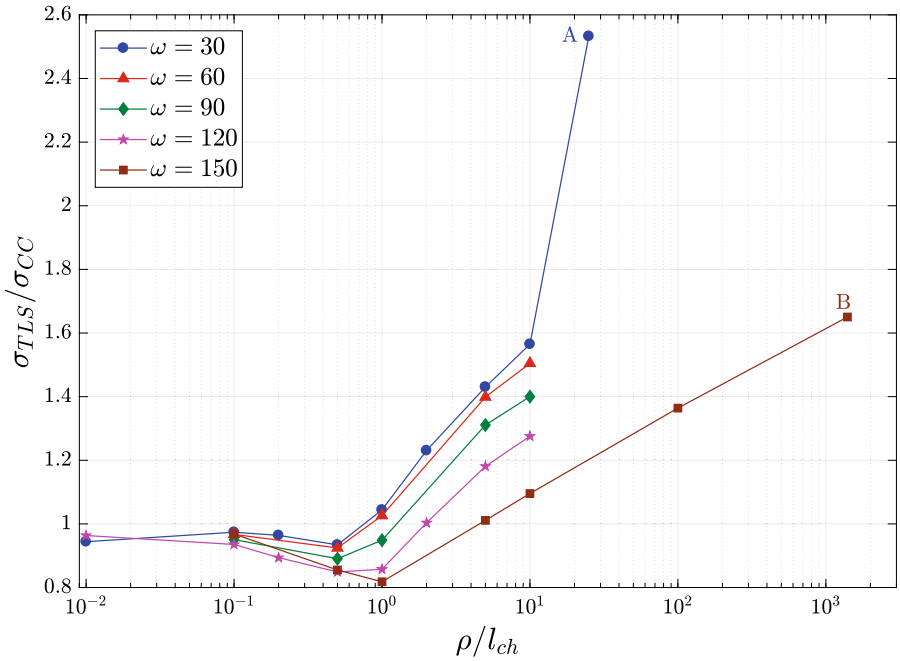

Fig. 17 Comparison between the apparent strengths predicted by the CC and the TLS approaches for a blunted V-notch: ($\sigma_{\mathrm{TLS}}/\sigma_{\mathrm{CC}}$) with respect to the relative fillet radius

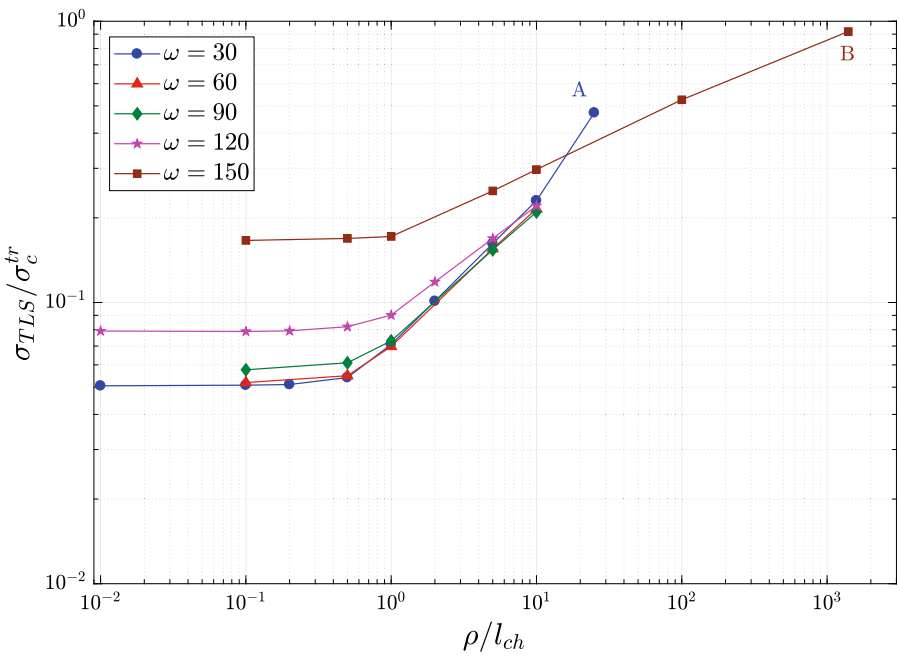

Fig. 18 Normalized TLS apparent strength for a blunted V-notch over the unnotched critical stress as a function of the relative fillet radius

For case A, the predicted TLS apparent strength is the same as for a cavity whereas for a case B, it is very close to the unnotched critical stress. We are thus confident in the TLS results even in the limit case of large fillet radii. On the other hand, the CC criterion being build on asymptotic considerations (fillet with infinite notch depth) is not able to give proper results for large fillet radii.

Finally, Fig. 20, shows a good agreement between CC, TLS and experimental data for a small fillet radius case.

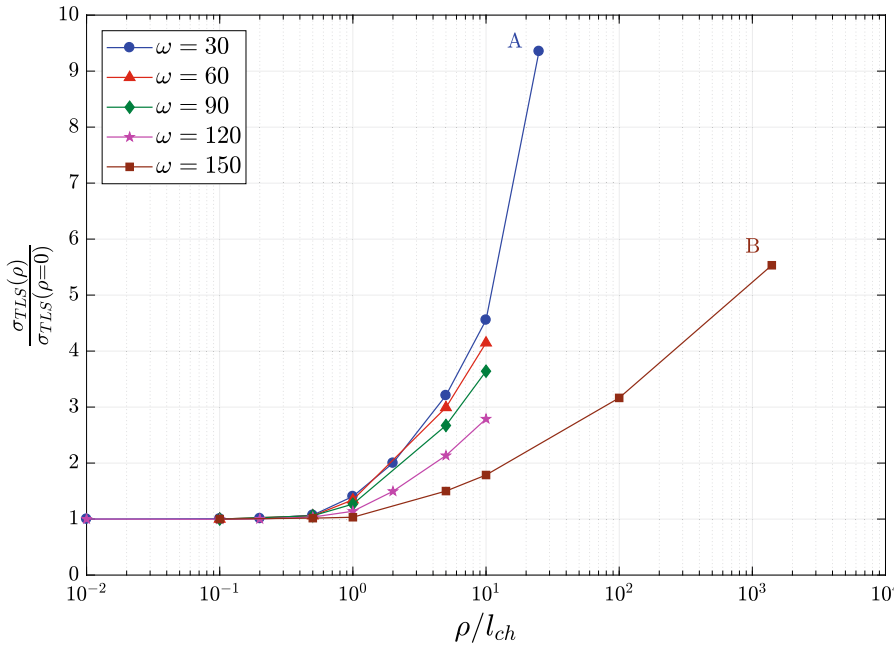

Fig. 19 TLS toughness improvement as a function of the relative fillet radius for different angles

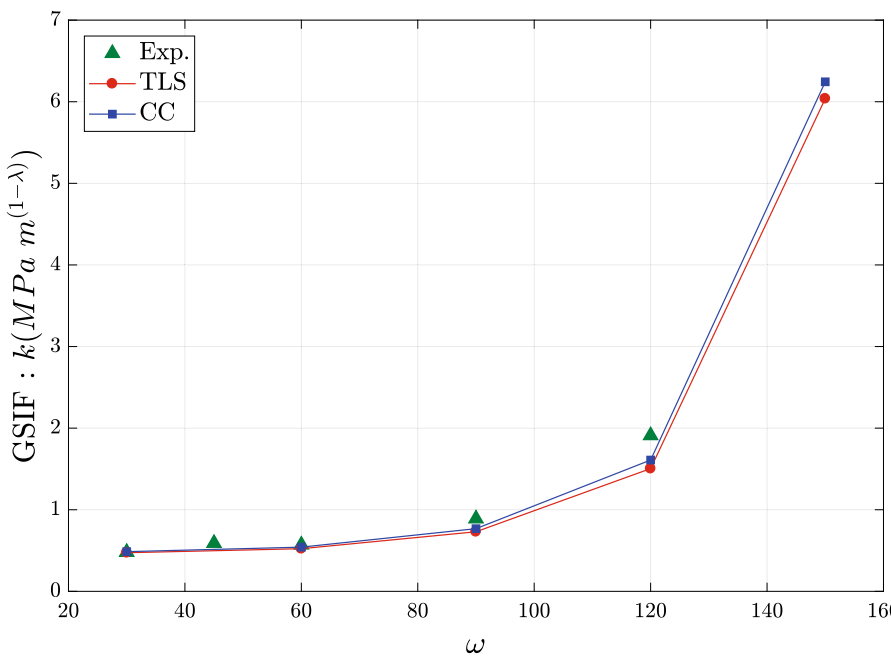

Fig. 20 Comparison of the evolution of GSIF obtained by the CC and TLS with those obtained experimentally (Dunn et al. 1997) as a function of the opening angle ω ($\rho/l_{ch} = 0.1$)

5.3 The cavity

We consider a cavity (Fig. 7) with radius ρ. We define the relative cavity radius as the ratio between the cavity radius and characteristic length of the material. The values of the apparent strength predicted by the coupled criterion and those issued from the TLS approach are close (Fig. 21) regardeless of the relative cavity radius. This can be explained by the fact that cavity does not induce structural singularity which is not the case for V-notches. We note that when the relative cavity radius becomes small the apparent strength becomes close to the unnotched critical stress. It means that when the cavity radius is small relatively to the

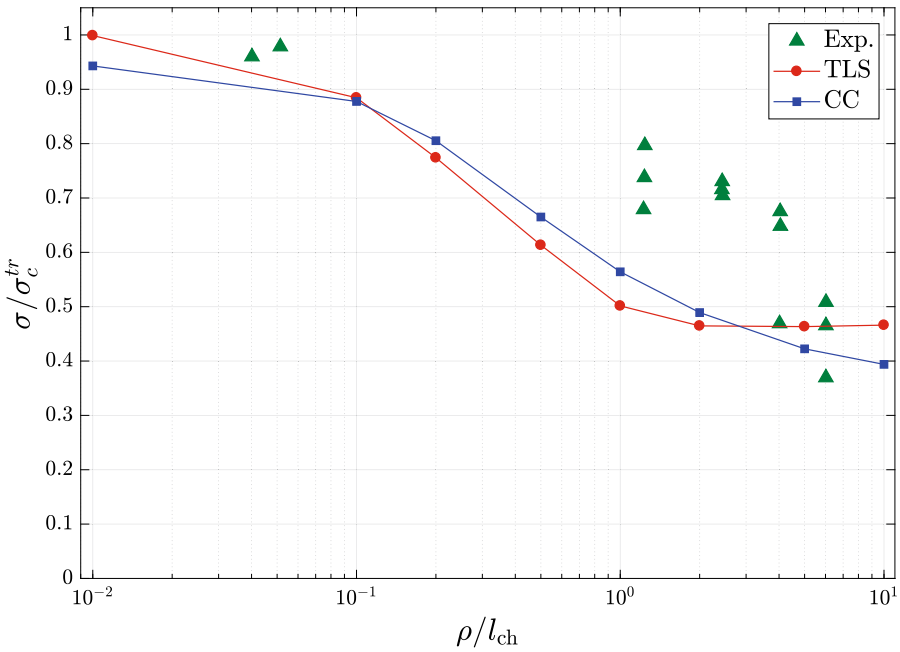

Fig. 21 Comparison between apparent strength for cavity predicted by coupled criterion, the TLS approach and those obtained experimentally (Li and Zhang 2006)

characteristic length, the structure strength is not influenced by the cavity. But, when the relative cavity radius becomes larger the apparent strength is smaller than the unnotched critical stress. When compared to experimental data, we observe an underestimation of both CC and TLS values especially for a radius in the range of the material length $\left(1 \leq \frac{\rho}{l_{ch}} < 10\right)$.

6 Conclusion

In this paper we have studied the effect of defects on the apparent strength of quasi-brittle specimen. Two approaches were considered: the coupled criterion (CC) and the Thick Level Set model (TLS). The first one uses pre-computed formulas based on asymptotic expansions whereas the second one is based on the evolution of the damage field with a dissipation control algorithm, the apparent strength being obtained by the peak stress.

Regarding the defects, we have considered notches (sharp or blunted) and cavities. In each case, we have considered a (semi)-infinite media. The non-finite domain is taking into account by mapping a layer of elements to infinity in the finite element simulation. For sharp notches, we have two lengths at stake: the notch depth and Irwin material length. For blunted V-notch, the fillet radius is a third length. Finally, for cavities, the lengths are the cavity radius and material length. We have thus not considered in the paper the effect of the specimen size but only the interaction between the defect size and material length.

The CC criteria are only applicable when the defect size is large compared to the material length. Within this range, the CC and TLS models give very close apparent strengths.

For the V-sharp notch, when the notch depth is large compared to the material length, CC and TLS apparent strength are very close and indicate that the more acute is the angle the less is the apparent strength. When the notch depth is the order of magnitude or smaller than the material length, CC and TLS predictions differ a lot. The TLS apparent strength tends to the material strength (as it should be since the notch becomes invisible within the material length) wheras the CC apparent is much too large and still sees the notch.

For the blunted V-notch, a very large notch depth has been considered compared to the material length. We have studied the interaction between the fillet radius and the material length. When the fillet radius is smaller than the material length, apparent CC and TLS strength are close to each other (and close to the sharp notch results). When the fillet radius is larger than the material length (and yet smaller than the notch depth), the TLS and CC differ. We are confident with the TLS

result since they match the the cavity case. When the fillet radius is much larger than the notch depth, we are also confident with the TLS results since the unnotched critical stress of the material is recovered.

For the cavity, the CC and TLS prediction are quite close to each other even when the material length is no longer negligible compared to the cavity radius. Both TLS and CC obtain the fact that when the cavity is becoming smaller than the material length, the apparent strength tends to the unnotched material critical stress. This is quite different from the V-notch case, for which only the TLS had this capacity. The CC criteria performs thus well on a wider range of (defect size / material size) for the cavity than for the V-notch. We note that in the cavity case, the fields are non singular.

Regarding the comparison with experimental data, a good agreement is obtained for the V-notch whereas a discrepancy is observed for both CC and TLS in the cavity case (when the radius is between 1 and 3 times the material length). Certainly further investigations are needed for that case.

Acknowledgements N.M., K.M., C.S. and J.Z. gratefully acknowledges the support of the ERC advanced Grant XLS no. 291102.

Appendix A: Details on the softening function and damage profile used in the TLS numerical simulations

The TLS model considered is given by:

$$g(d) = 2\sqrt{1-d} \tag{61}$$

$$\tilde{h}(d,\lambda_c) = \frac{d}{(\sqrt{1-d}+\lambda_c(1-\sqrt{1-d})^2)^2} \tag{62}$$

where λ_c is a dimensionless parameter defined as the ratio between the TLS thickness ($2l_c$) and the cohesive zone length:

$$\lambda_c = \frac{2l_c}{Ew_c/\sigma_c} \tag{63}$$

The above choice (61) corresponds to a linear cohesive relation [already considered in Gómez et al. (2015)]. Indeed, inserting $g(d)$ into (27), we get:

$$\sigma = \sigma_c\sqrt{1-d}\sqrt{\frac{\tilde{h}(d)}{d}} \tag{64}$$

$$w = \frac{2\sigma_c l_c}{E}(1-\sqrt{1-d})^2\sqrt{\frac{\tilde{h}(d)}{d}} \tag{65}$$

Eliminating d in the above yields:

$$\frac{\sigma}{\sigma_c} = 1 - \frac{w}{w_c} \tag{66}$$

The toughness is given by:

$$G_c = \frac{1}{2}\sigma_c w_c \tag{67}$$

The following data for PMMA are used:

$$E = 3500 \text{ MPa}, \nu = 0.3, \sigma_c = 70 \text{ MPa},$$
$$Gc = 3.5\ 10^{-4} \text{ MPa m} \tag{68}$$

This implies:

$$l_{ch} = 2.5\times10^{-4} \text{ m},\ w_c = 2G_c/\sigma_c = 10^{-5} \text{ m},$$
$$l_c = \frac{Ew_c}{2\sigma_c}\lambda_c = 2.5\times10^{-4}\,\lambda_c \text{ m} \tag{69}$$

Regarding the choice for λ_c, it needs to be less or equal to 0.5 (Gómez et al. 2015) otherwise the convexity requirement of $\tilde{h}$ is not satisfied. We consider:

$$\lambda_c = 0.2 \tag{70}$$

leading to

$$l_c = 5\times10^{-5} \tag{71}$$

Note that for a more general cohesive law

$$f_{coh}\left(\frac{\sigma}{\sigma_c}, \frac{w}{w_c}\right) = 0$$

the function $\tilde{h}(d,\lambda_c)$ is obtained as the solution to the equation

$$f_{coh}\left(\sqrt{1-d}\sqrt{\frac{\tilde{h}(d,\lambda_c)}{d}}, \lambda_c(1-\sqrt{1-d})^2\sqrt{\frac{\tilde{h}(d,\lambda_c)}{d}}\right) = 0.$$

Conditions (7) imply some restrictions on the choice of f_{coh} and λ_c.

Appendix B: Generalized stress intensity factor for an edge notch in an infinite medium

The generalized stress intensity factor k at the tip of a notch with depth a in an infinite medium subjected to a prescribed tension σ_∞ is given by:

$$k = \kappa \sigma_\infty a^{1-\lambda} \tag{72}$$

where the parameter κ is given in Table 2 one has to keep in mind the normalization proposed in Sect. 2.1. For the crack ($\omega = 0$) with the usual normalization of the mode I eigenvector, it gives $\kappa' = 1.119$ to be compared to the coefficient 1.122 proposed by Tada et al. (2000).

Table 2 Data to compute the generalized stress intensity factor at a single edge notch in an infinite medium

ω	λ	κ
0	0.500	0.791
30	0.502	0.797
60	0.512	0.831
90	0.545	0.924
120	0.616	1.071
150	0.752	1.237
165	0.858	1.247

Appendix C: Data for the coupled criterion—cases of sharp and blunted V-notch

The scalar λ is the root of the equation:

$$\sin(\lambda\beta) + \lambda \sin\beta = 0, \quad \beta = 2\pi - \omega \tag{73}$$

whereas values of $A^\star$ derive from an asymptotic procedure carried out with respect to the small crack extension length l_{CC} (Leguillon 2002). The values found in this reference are made dimensionless multiplying by $E/(1-\nu^2)$. Moreover, keep in mind again the normalization of the eigenvector in Sect. 4.1 (Fig. 22).

Similarly $B^\star$ and $C^\star$ derive from an asymptotic procedure but carried out with respect to the notch root radius ρ. The $B^\star$ and $C^\star$ coefficients were computed for a Young modulus $E = 2300$ MPa and a Poisson ratio $\nu = 0.3$ and then multiplied by $E/(1-\nu^2)$. As $A^\star$, they are functions of ω and in addition they depend also on the dimensionless crack length $\zeta = l_{CC}/\rho$ which plays the role of a parameter in the model involving both lengths ρ and l_{CC}. It is illustrated in Figs. 23 and 24. Attention is drawn to the fact that $C^\star$ only slightly

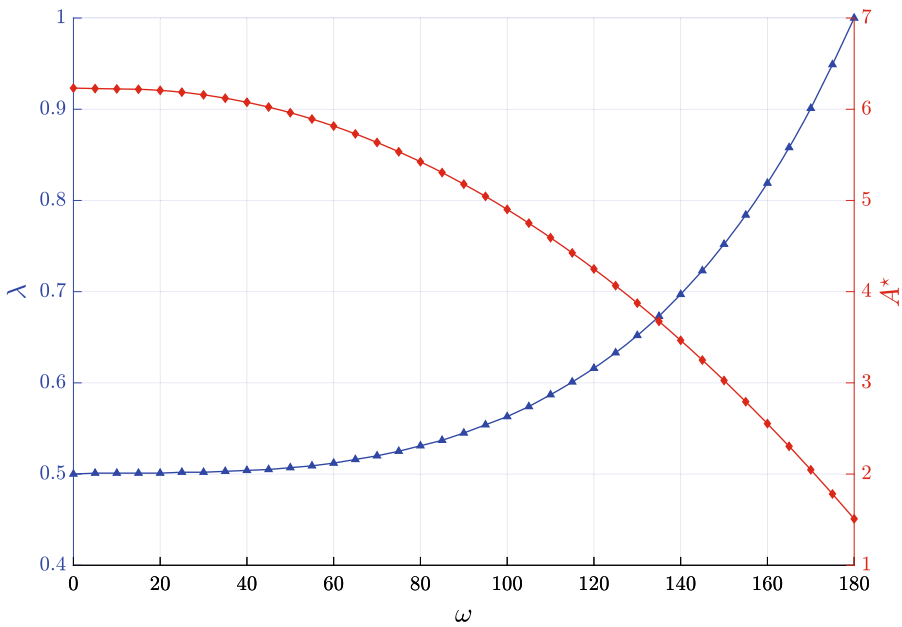

Fig. 22 $A^\star$ (Diamond) and λ (Triangle) function of the opening angle ω

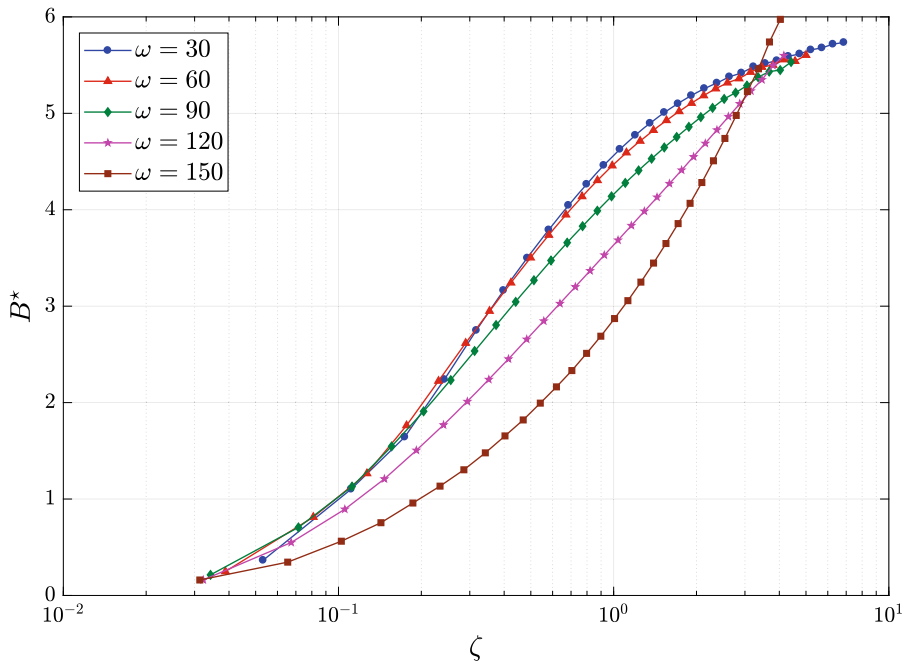

Fig. 23 $B^\star$ and λ function of the dimensionless length ζ

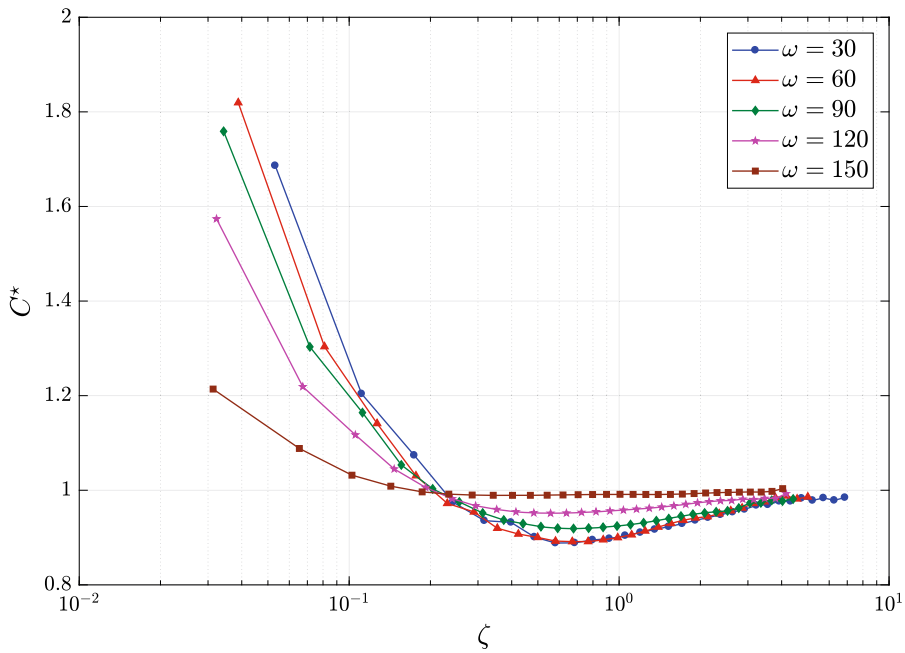

Fig. 24 $C^\star$ and λ function of the dimensionless length ζ

deviates from 1 except for small values of ζ. This later case corresponds to large root radii compared to the crack length at initiation. At the limit it falls outside the scope of the asymptotic expansion used here which assumes that the two small parameters ρ and l_{CC} are of the same order of magnitude. A different procedure has to be employed (Tables 3, 4, 5, 6, 7).

Table 3 Influence of the opening angle ω on the singularity strength at a V-notch in mode I and coefficient $A^\star$ computed for a Poisson ratio $\nu = 0.3$

As long as ν stays in the range 0.1–0.4, values above do not change

ω (deg.)	λ	$A^\star$	ω (deg.)	λ	$A^\star$
0	0.500	6.232	95	0.554	5.045
5	0.501	6.227	100	0.563	4.902
10	0.501	6.223	105	0.574	4.751
15	0.501	6.219	110	0.587	4.592
20	0.501	6.207	115	0.601	4.425
25	0.502	6.187	120	0.616	4.249
30	0.502	6.158	125	0.633	4.066
35	0.503	6.121	130	0.652	3.874
40	0.504	6.077	135	0.673	3.674
45	0.505	6.024	140	0.697	3.466
50	0.507	5.962	145	0.723	3.250
55	0.509	5.893	150	0.752	3.026
60	0.512	5.816	155	0.784	2.793
65	0.516	5.730	160	0.819	2.553
70	0.520	5.636	165	0.858	2.304
75	0.525	5.534	170	0.901	2.047
80	0.531	5.424	175	0.949	1.782
85	0.537	5.306	180	1.000	1.509
90	0.545	5.179			

Table 4 Variations of the coefficients $B^\star$ and $C^\star$ for a blunted V-notch for different opening angles ω

$\omega = 30°$			$\omega = 60°$			$\omega = 90°$		
ζ	$B^\star$	$C^\star$	ζ	$B^\star$	$C^\star$	ζ	$B^\star$	$C^\star$
6.864	5.7348	0.985	5.613	5.656	0.979	5.000	5.603	0.986
6.266	5.7175	0.979	5.124	5.618	0.977	4.564	5.540	0.982
5.715	5.6789	0.984	4.674	5.620	0.988	4.163	5.557	0.988
5.209	5.6582	0.978	4.260	5.593	0.983	3.795	5.501	0.984
4.743	5.6160	0.983	3.879	5.544	0.985	3.455	5.480	0.976
4.315	5.5914	0.977	3.529	5.523	0.974	3.143	5.428	0.972
3.921	5.5466	0.977	3.206	5.487	0.971	2.856	5.360	0.962
3.558	5.5176	0.969	2.910	5.437	0.964	2.592	5.317	0.957
3.224	5.4835	0.968	2.637	5.393	0.956	2.349	5.256	0.950
2.917	5.4189	0.960	2.386	5.339	0.947	2.125	5.184	0.944
2.635	5.3790	0.954	2.155	5.272	0.940	1.919	5.106	0.941
2.375	5.3144	0.948	1.942	5.197	0.933	1.730	5.020	0.937
2.136	5.2576	0.942	1.747	5.119	0.926	1.556	4.927	0.930
1.916	5.1838	0.936	1.567	5.024	0.920	1.396	4.825	0.922
1.714	5.0997	0.929	1.402	4.922	0.912	1.248	4.713	0.914
1.528	5.0094	0.923	1.249	4.808	0.906	1.113	4.592	0.906
1.356	4.8973	0.917	1.109	4.678	0.900	0.988	4.457	0.900
1.199	4.7728	0.911	0.980	4.533	0.894	0.873	4.305	0.895

Table 4 continued

$\omega = 30°$			$\omega = 60°$			$\omega = 90°$		
ζ	$B^\star$	$C^\star$	ζ	$B^\star$	$C^\star$	ζ	$B^\star$	$C^\star$
1.054	4.6275	0.904	0.862	4.373	0.889	0.768	4.138	0.892
0.921	4.4610	0.898	0.753	4.183	0.889	0.671	3.948	0.891
0.798	4.2649	0.895	0.653	3.976	0.888	0.581	3.738	0.893
0.685	4.0464	0.889	0.560	3.735	0.893	0.499	3.502	0.900
0.581	3.7915	0.888	0.475	3.495	0.895	0.423	3.243	0.907
0.486	3.4996	0.901	0.397	3.180	0.916	0.354	2.949	0.920
0.398	3.1634	0.932	0.325	2.843	0.927	0.290	2.617	0.954
0.317	2.7491	0.936	0.259	2.442	0.957	0.231	2.224	0.972
0.243	2.2400	0.975	0.198	2.032	1.017	0.177	1.763	1.031
0.174	1.6431	1.074	0.142	1.517	1.114	0.127	1.265	1.141
0.111	1.1025	1.204	0.091	0.980	1.268	0.081	0.812	1.304
0.053	0.36496	1.686	0.044	0.302	1.768	0.039	0.249	1.819

Table 5 Variations of the coefficients $B^\star$ and $C^\star$ for a blunted V-notch for different opening angles ω

$\omega = 90°$			$\omega = 120°$			$\omega = 150°$		
ζ	$B^\star$	$C^\star$	ζ	$B^\star$	$C^\star$	ζ	$B^\star$	$C^\star$
4.414	5.532	0.982	4.155	5.599	0.993	4.035	5.974	1.003
4.029	5.449	0.977	3.793	5.496	0.983	3.684	5.740	0.998
3.676	5.433	0.979	3.460	5.348	0.983	3.360	5.462	0.996
3.350	5.374	0.973	3.153	5.231	0.980	3.063	5.225	0.996
3.051	5.288	0.973	2.871	5.100	0.981	2.789	4.978	0.996
2.775	5.214	0.962	2.612	4.966	0.978	2.537	4.740	0.995
2.521	5.150	0.956	2.373	4.827	0.978	2.305	4.508	0.995
2.288	5.057	0.954	2.154	4.688	0.976	2.092	4.282	0.994
2.074	4.961	0.952	1.952	4.549	0.974	1.896	4.067	0.993
1.876	4.860	0.949	1.766	4.411	0.970	1.715	3.856	0.992
1.695	4.755	0.945	1.595	4.271	0.967	1.549	3.650	0.991
1.527	4.646	0.940	1.438	4.130	0.965	1.396	3.447	0.991
1.374	4.529	0.936	1.293	3.984	0.962	1.256	3.249	0.991
1.232	4.408	0.931	1.160	3.836	0.960	1.127	3.057	0.991
1.102	4.278	0.927	1.037	3.684	0.958	1.008	2.872	0.991
0.982	4.139	0.924	0.925	3.530	0.956	0.898	2.689	0.991
0.872	3.990	0.922	0.821	3.368	0.955	0.797	2.511	0.991
0.771	3.830	0.920	0.726	3.201	0.953	0.705	2.332	0.991
0.678	3.658	0.919	0.638	3.027	0.952	0.620	2.163	0.990
0.592	3.474	0.920	0.557	2.846	0.951	0.541	1.995	0.990
0.513	3.269	0.923	0.483	2.656	0.952	0.469	1.820	0.989
0.441	3.045	0.929	0.415	2.452	0.954	0.403	1.655	0.989
0.374	2.805	0.937	0.352	2.240	0.959	0.342	1.479	0.989
0.312	2.535	0.952	0.294	2.011	0.967	0.286	1.303	0.990
0.256	2.233	0.975	0.241	1.769	0.982	0.234	1.134	0.992

Table 5 continued

$\omega = 90^\circ$			$\omega = 120^\circ$			$\omega = 150^\circ$		
ζ	$B^\star$	$C^\star$	ζ	$B^\star$	$C^\star$	ζ	$B^\star$	$C^\star$
0.204	1.909	1.003	0.192	1.505	1.006	0.186	0.958	0.997
0.156	1.546	1.054	0.147	1.209	1.045	0.143	0.754	1.009
0.112	1.129	1.164	0.105	0.894	1.117	0.102	0.563	1.032
0.072	0.706	1.303	0.067	0.549	1.219	0.065	0.346	1.088
0.034	0.214	1.759	0.032	0.161	1.574	0.031	0.160	1.214

Table 6 Variations of the coefficients $\tilde{B}^\star$ and $\tilde{C}^\star$ as functions of ratio $\left(\frac{\rho}{l_{ch}}\right)$, for a blunted V-notch with different opening angles ω

$\omega = 30^\circ$			$\omega = 60^\circ$			$\omega = 90^\circ$		
$\frac{\rho}{l_{ch}}$	$\tilde{B}^\star$	$\tilde{C}^\star$	$\frac{\rho}{l_{ch}}$	$\tilde{B}^\star$	$\tilde{C}^\star$	$\frac{\rho}{l_{ch}}$	$\tilde{B}^\star$	$\tilde{C}^\star$
00.01	5.838466	1.019665	00.01	5.975091	0.993725	00.01	6.058896	1.016498
00.10	5.246229	0.941309	00.10	5.253511	0.938465	00.10	5.184388	0.944289
00.20	4.737609	0.909074	00.20	4.731730	0.902033	00.20	4.656840	0.910152
00.50	3.789560	0.888524	00.50	3.794421	0.891915	00.50	3.751435	0.892467
01.00	3.027783	0.933278	01.00	3.042057	0.920617	01.00	3.010784	0.917139
02.00	2.254711	0.973674	02.00	2.332763	0.973295	02.00	2.303579	0.968565
05.00	1.520780	1.103373	05.00	1.535525	1.110634	05.00	1.541878	1.079652
10.00	1.086429	1.214402	10.00	1.152760	1.218436	10.00	1.120037	1.193169

Table 7 Variations of the coefficients $\tilde{B}^\star$ and $\tilde{C}^\star$ as functions of ratio $\left(\frac{\rho}{l_{ch}}\right)$, for a blunted V-notch with different opening angles ω

$\omega = 90^\circ$			$\omega = 120^\circ$			$\omega = 150^\circ$		
$\frac{\rho}{l_{ch}}$	$\tilde{B}^\star$	$\tilde{C}^\star$	$\frac{\rho}{l_{ch}}$	$\tilde{B}^\star$	$\tilde{C}^\star$	$\frac{\rho}{l_{ch}}$	$\tilde{B}^\star$	$\tilde{C}^\star$
00.01	6.116479	1.011826	00.01	6.234500	1.053982	00.01	7.381271	1.038309
00.10	5.016597	0.953375	00.10	4.784224	0.977233	00.10	4.600453	0.995193
00.20	4.417471	0.931522	00.20	4.051936	0.963207	00.20	3.613970	0.991118
00.50	3.542691	0.919448	00.50	3.151815	0.952842	00.50	2.603411	0.991119
01.00	2.855123	0.935450	01.00	2.525814	0.953559	01.00	2.009838	0.989572
02.00	2.205624	0.977672	02.00	1.963606	0.970159	02.00	1.537157	0.989348
05.00	1.501323	1.065434	05.00	1.356627	1.025487	05.00	1.059033	0.993813
10.00	1.086623	1.178068	10.00	0.989467	1.095157	10.00	0.765125	1.007979

Appendix D: Data for the coupled criterion—cavity

See Figs. 25, 26 and Tables 8, 9, 10.

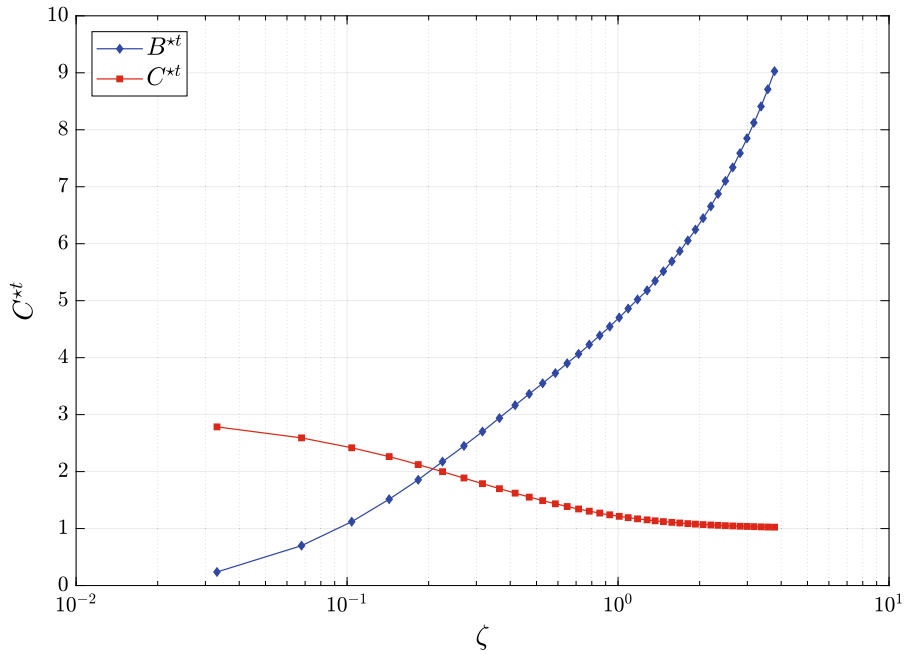

Fig. 25 $B^{\star \mathrm{t}}$ and $C^{\star \mathrm{t}}$ function of the dimensionless length ζ

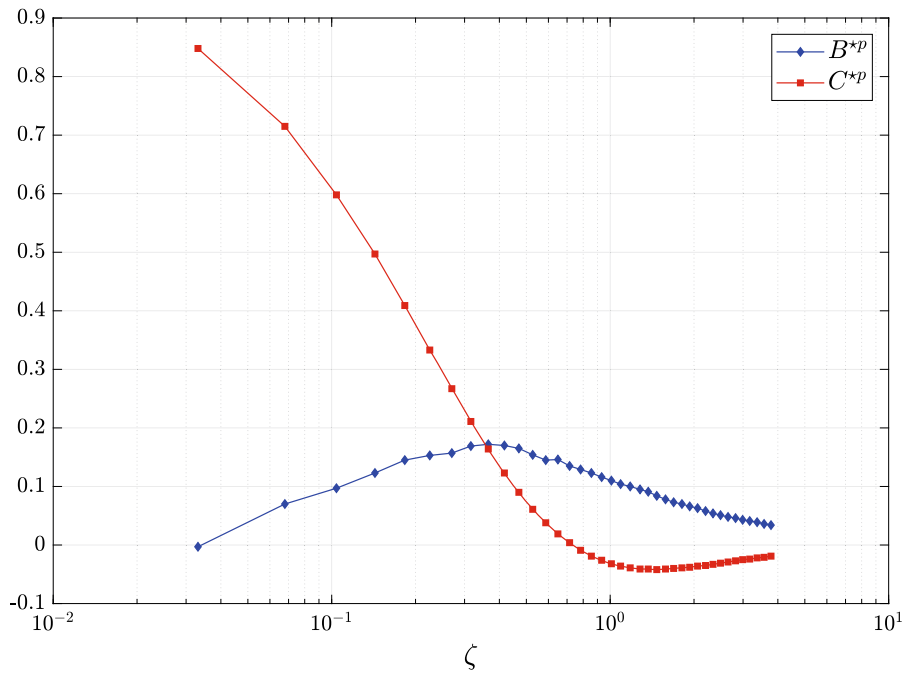

Fig. 26 $B^{\star \mathrm{p}}$ and $C^{\star \mathrm{p}}$ function of the dimensionless length ζ

Table 8 $B^{\star t}$ and, $C^{\star t}$ as functions of the dimensionless length ζ for a cavity

Tensile loading					
ζ	$B^{\star t}$	$C^{\star t}$	ζ	$B^{\star t}$	$C^{\star t}$
3.78	9.029	1.025	1.01	4.704	1.215
3.57	8.711	1.027	0.932	4.545	1.242
3.37	8.409	1.03	0.856	4.389	1.272
3.17	8.123	1.034	0.783	4.229	1.305
2.99	7.849	1.037	0.715	4.066	1.344
2.82	7.589	1.041	0.649	3.901	1.387
2.65	7.339	1.046	0.587	3.729	1.435
2.49	7.101	1.051	0.527	3.55	1.49
2.34	6.874	1.057	0.47	3.363	1.552
2.2	6.656	1.063	0.417	3.165	1.622
2.06	6.448	1.07	0.365	2.939	1.7
1.93	6.247	1.078	0.316	2.703	1.788
1.81	6.055	1.087	0.27	2.452	1.888
1.69	5.87	1.098	0.225	2.175	1.999
1.58	5.69	1.109	0.183	1.856	2.123
1.47	5.516	1.122	0.143	1.515	2.263
1.37	5.347	1.136	0.104	1.12	2.418
1.28	5.18	1.153	0.0679	0.7	2.592
1.18	5.022	1.171	0.0331	0.238	2.785
1.09	4.861	1.192			

Table 9 $B^{\star p}$ and $C^{\star p}$ as functions of the dimensionless length ζ for a cavity in compression p for compression. One can note a small inaccuracy in the penultimate line since $B^{\star p}$ cannot be negative

Compression loading					
ζ	$B^{\star p}$	$C^{\star p}$	ζ	$B^{\star p}$	$C^{\star p}$
3.78	0.034	− 0.019	1.01	0.11	− 0.032
3.57	0.036	− 0.021	0.932	0.116	− 0.026
3.37	0.039	− 0.022	0.856	0.123	− 0.019
3.17	0.041	− 0.024	0.783	0.129	− 0.009
2.99	0.043	− 0.025	0.715	0.135	0.004
2.82	0.046	− 0.027	0.649	0.146	0.019
2.65	0.048	− 0.029	0.587	0.145	0.038
2.49	0.051	− 0.031	0.527	0.154	0.061
2.34	0.054	− 0.033	0.47	0.165	0.09
2.2	0.058	− 0.035	0.417	0.17	0.123
2.06	0.063	− 0.036	0.365	0.172	0.164
1.93	0.066	− 0.038	0.316	0.169	0.211

Table 9 continued

Compression loading					
ζ	$B^{\star p}$	$C^{\star p}$	ζ	$B^{\star p}$	$C^{\star p}$
1.81	0.07	− 0.039	0.27	0.157	0.267
1.69	0.073	− 0.04	0.225	0.153	0.333
1.58	0.078	− 0.041	0.183	0.145	0.409
1.47	0.084	− 0.042	0.143	0.123	0.497
1.37	0.091	− 0.041	0.104	0.097	0.598
1.28	0.095	− 0.041	0.0679	0.07	0.715
1.18	0.1	− 0.039	0.0331	− 0.003	0.848
1.09	0.104	− 0.036			

Table 10 Variations of the coefficients $\tilde{B}^{\star t/p}$ and $\tilde{C}^{\star t/p}$ as functions of the dimensionless ratio $\frac{\rho}{l_{ch}}$ for a cavity under tension

Tensile loading			Compression loading		
$\frac{\rho}{l_{ch}}$	$\tilde{B}^{\star t}$	$\tilde{C}^{\star t}$	$\frac{\rho}{l_{ch}}$	$\tilde{B}^{\star p}$	$\tilde{C}^{\star p}$
0.01	11.278	1.0109	0.01	− 0.13146	0.14646
0.1	6.0607	1.0867	0.1	− 0.12963	0.14463
0.2	4.9152	1.1849	0.2	− 0.1276	0.1426
0.5	3.7341	1.4336	0.5	− 0.12152	0.13652
1	2.9677	1.6901	1	− 0.11138	0.12638
2	2.2911	1.9525	2	− 0.091098	0.1061
5	1.5284	2.2575	5	− 0.030258	0.045258
10	1.1026	2.4252	10	0.11239	− 0.02961
100	0.39479	2.7195	100	0.102	0.57858

References

Bazant ZP, Belytschko TB, Chang TP (1984) Continuum theory for strain-softening. J Eng Mech ASCE 110(12):1666–1692

Bernard P-E, Moës N, Chevaugeon N (2012) Damage growth modeling using the Thick Level Set (TLS) approach: efficient discretization for quasi-static loadings. Comput Methods Appl Mech Eng 233–236:11–27

Carpinteri A, Cornetti P, Pugno N, Sapora A, Taylor D (2008) A finite fracture mechanics approach to structures with sharp V-notches. Eng Fract Mech 75(7):1736–1752

Cloirec M (2005) Application of X-FEM for multi-scale problems and parallel computations. Theses, Ecole Centrale de Nantes (ECN); Université de Nantes

Dunn ML, Suwito W, Cunningham S, May CW (1997) Fracture initiation at sharp notches under mode I, mode II, and mild mixed mode loading. Int J Fract 84(4):367–381

Frémond M, Stolz C (2017) On alternative approaches for graded damage modelling. In: Frémond M, Maceri F, Vairo G (eds) Models, simulation and experimental issues in structural

mechanics, vol 8. Solids and structural mechanics. Springer, Cham, pp 87–104
Gómez AP (2015) Coupled numerical and analytical analysis of a graduated damage model. Theses, Ecole Centrale de Nantes (ECN)/Université Nantes Angers Le Mans
Gómez FJ, Elices M (2003) A fracture criterion for sharp V-notched samples. Int J Fract 123(3):163–175
Gómez FJ, Elices M (2004) A fracture criterion for blunted V-notched samples. Int J Fract 127(3):239–264
Gómez A-P, Moës N, Stolz C (2015) Comparison between thick level set (TLS) and cohesive zone models. Adv Model Simul Eng Sci 2(18):1–22
Irwin GR (1968) Linear fracture mechanics, fracture transition, and fracture control. Eng Fract Mech 1(2):241–257
Leguillon D (2002) Strength or toughness? A criterion for crack onset at a notch. Eur J Mech A Solids 21(1):61–72
Lions P-L (1982) Generalized solutions of Hamilton–Jacobi equations. Pitman Advanced Publishing Program, Boston
Leguillon D, Quesada D, Putot C, Martin E (2007) Prediction of crack initiation at blunt notches and cavities? Size effects. Eng Fract Mech 74:2420–2436
Leguillon D, Yosibash Z (2003) Crack onset at a v-notch. Influence of the notch tip radius. Int J Fract 122(1/2):1–21
Li J, Zhang XB (2006) A criterion study for non-singular stress concentrations in brittle or quasi-brittle materials. Eng Fract Mech 73(4):505–523
Moreau K, Moës N, Chevaugeon N, Salzman A (2017) Concurrent development of local and non-local damage with the thick level set approach: implementation aspects and application to quasi-brittle failure. Comput Methods Appl Mech Eng 327:306–326
Moës N, Stolz C, Bernard P-E, Chevaugeon N (2011) A level set based model for damage growth: the thick level set approach. Int J Numer Methods Eng 86:358–380
Moës N, Stolz C, Chevaugeon N (2014) Coupling local and non-local damage evolution with the Thick Level Set model. Adv Model Simul Eng Sci 2(16):21
Picard D, Leguillon D, Putot C (2006) A method to estimate the influence of the notch-root radius on the fracture toughness measurement of ceramics. J Eur Ceram Soc 26(8):1421–1427
Sethian JA (1999) Level set methods and fast marching methods: evolving interfaces in computational geometry, fluid mechanics, computer vision and material science. Cambridge University Press, Cambridge
Stolz C (2016) On moving thick layer approach for graded damage modelling. Int J Fract 202(2):195–205
Tada H, Paris PC, Irwin GR (2000) The stress analysis of cracks handbook, 3rd edn. ASME Press, New York
Williams ML (1952) Stress singularities resulting from various boundary conditions in angular corners of plates in extension. J Appl Mech Trans ASME 19:526–528